

# JCU ePrints

This file is part of the following reference:

**Cole, David (2007) *The splashing morphology of liquid-liquid impacts.*  
PhD thesis, James Cook University.**

Access to this file is available from:

<http://eprints.jcu.edu.au/2065>



# CHAPTER 1 - LITERATURE REVIEW

## 1.1 Introduction

One of the most pleasant sensations one can experience is the smell of fresh rain and the rather hypnotic rhythm of the raindrops splashing. The ubiquitous nature of falling rain means that we rarely pause to think about the phenomena behind the sound and splash we both hear and see. Everybody understands that when a raindrop impacts on a liquid surface, ripples propagate and sound radiates from the impact site. However, what the human eye cannot see is the intricate interaction of surface tension, viscosity and inertia that combine to create the fascinating and beautiful splashing event. Broadly speaking, a liquid-liquid impact can result in a range of complex phenomena such as cavity formation, bubble entrapment, jetting and vortex ring formation. The difficulty in studying these events arises from the fact that they occur with exceptionally short timescales, ranging from microseconds to milliseconds. Many attempts have been made to capture the splashing from a liquid-liquid impact for over 100 years. However, the technology to continuously record video images at high framing rates over relatively long periods has been lacking. It has only been in the last decade that technology has become sufficiently advanced that these millisecond events can be captured in their entirety. In this thesis, advanced digital video and laser technology will be used to study some of the phenomena occurring in liquid-liquid impacts.

## 1.2 Thesis Focus

This thesis will broadly focus on understanding the fundamental fluid mechanics governing the various splashing phenomena from liquid-liquid impacts. The motivation for conducting such a study comes from the need to understand splashing behaviour in many industrial and natural applications. Some of the industrial processes include gas injection during metallurgical processes (Liow *et al.* 1994), coating of metallic products (Mehdi-Nejad *et al.* 2003), fire suppression systems (Manzello and Yang 2003) and the entrapment of bubbles by falling drops into superheated liquids to enhance boiling (Carroll and Mesler 1981). Liquid splashing also has a significant role in many natural processes including soil erosion (Ellison 1944), transport of bacteria (Fitt and Shaw 1989), water aeration (Morton and Cresswell 1992) and jetting during meteorite impacts. In many of these applications, the ways in which the cavity expands and

collapses influences much of the flow behaviour including jetting. In other applications, the entrapment of air bubbles from impacting liquid drops may be either desirable or undesirable depending on the situation. In water aeration for aquaculture, rivers, lakes and even the world's oceans, the entrapment of air by an impacting liquid drops helps increase the dissolved oxygen levels, via mass transfer, within the water. However, in industrial processes, such as spray coating, the entrapment of air under the impacting liquid drop can cause undesirable effects that lead to the coating being applied unevenly. In food processing the inclusion of excessive amounts of air can assist bacterial growth and render the product unsuitable for consumption. Just from these few examples, we can see how the formation of bubbles and jets in liquid-liquid impacts is of immediate practical relevance. Therefore, in this study we seek to gain a deeper fundamental understanding of the liquid-liquid impact process in such areas as cavity development, jetting and bubble entrapment.

### **1.3 Background**

A falling liquid drop can either impact on a liquid or solid surface. The resulting splashing behaviour is vastly different depending on which of these two surfaces the drop impacts. Therefore, this thesis will focus on liquid-liquid impacts and the fluid dynamics of liquid-solid impacts will not be considered here. The types of liquid-liquid impacts people are most familiar with is the impact of a raindrop in a pool of water, like a lake. In this situation, the drops impact near their terminal velocity and give rise to specific flow behaviours. These specific behaviours may include secondary drop formation during the initial stages of the impact or crown formation as it is more commonly known, bubbles may be left on the surface, and some audible noise may be heard. What most observers do not understand is the phenomena will vary markedly depending on the depth of the pool and the velocity at which the impact occurs. In fact, in low velocity impacts it is possible that no secondary drops will be formed, no jetting will occur and no audible noise will be apparent. However other flow behaviour like air entrapment and vortex ring formation may occur. Furthermore, the depth of the pool may completely inhibit all the aforementioned behaviour. Thus, the field of liquid-liquid impacts can be further broken down into three main subcategories, deep pools, shallow pools and thin films. These subcategories can be further broken down into a series of regimes based on impact velocity. The effect of pool depth will now be discussed.

The actual definition of what constitutes a deep pool, shallow pool or thin film is usually put in the form of a dimensionless ratio of the pool depth ( $h_{pool}$ ) to drop diameter ( $d_d$ ). Table 1.1 highlights the boundaries between each of these regions.

**Table 1.1** Classification of pool depth

Deep Pools	Shallow Pools	Thin Films
$h_{pool}/d_d \gg 1$	$h_{pool}/d_d \approx 1$	$h_{pool}/d_d \ll 1$

A deep pool is considered to have a depth many times greater than the characteristic length (drop diameter) of the liquid object impacting on it. A classic example of this is a raindrop impacting on a large body of water like a lake. Deep pools have the benefit of the splashing phenomena being free from any boundary effects due to the influence of the pool bottom thereby simplifying the problem. In this thesis only deep pool impacts will be considered. Shallow pools on the other hand have a depth approximately equal to the length scale of the impacting object, an example being rain impacting on a puddle. The close proximity of the bottom surface to the impact site alters the subsequent cavity formation dynamics dramatically when compared to deep pools (Vander-Wal *et al.* 2006). Finally, thin films have a depth many times smaller than that of the impacting liquid (e.g. spray coating of metals). Thin film problems approach that of liquid-solid type problems and therefore share many of the same characteristics.

The first studies of liquid-liquid impacts in relatively deep pools were performed by Reynolds (1875, 1881), Thomson (1885), and Worthington (1897, 1900, 1908). Worthington was the first to conduct a systematic investigation into liquid-liquid splash. This, now classical, series of experiments was the first to uncover the complex and beautiful way in which drops impact on liquid surfaces (Worthington 1908). Through the novel use of spark flash photography Worthington was able to capture stunning images of drops splashing. Since Worthington's first attempts, many more features associated with splashing have been identified and classified by numerous authors (Rein 1993, 1996; Morton *et al.* 2000; Liow 2001). The subsequent cavity dynamics are a balance between the impact kinetic energy ( $\rho_d U_d^2 / 2$ ), the gravitational potential energy of the drop ( $\rho_d g d_d$ ) and surface energy. A summary of the current known phenomena from liquid drops impacting on deep liquid pools is shown in Figure 1.1.

The phenomena are subdivided into a series of regimes based on the Froude number ( $Fr = U^2/gL$ ).

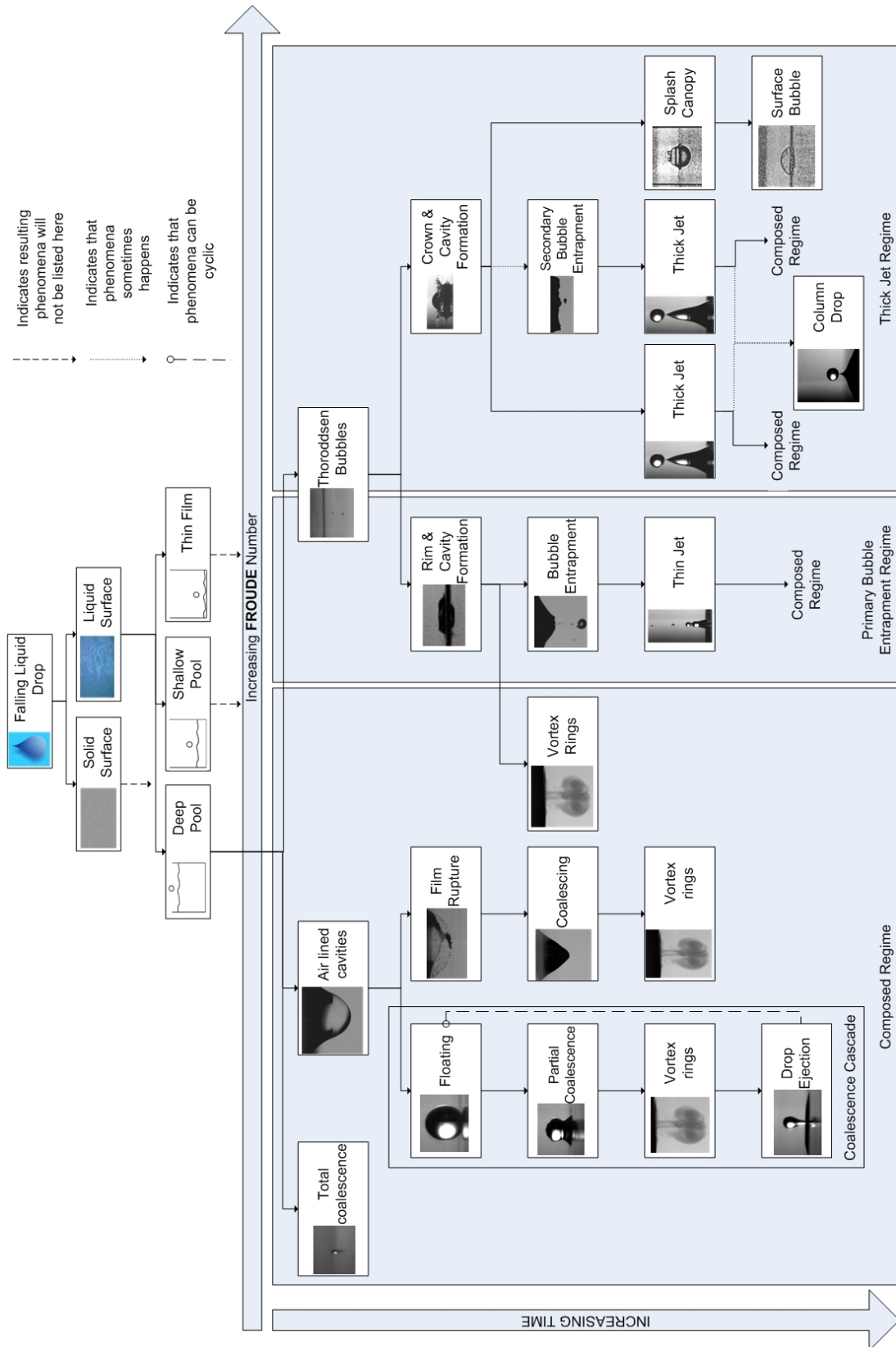


Figure 1.1 Map of phenomena associated with liquid-liquid impact (Cole 2007)

The first regime encountered is the so called composed regime after Fedorchenko and Wang (2004). Other authors (Rein 1996) have sought to describe this regime in terms of floating, bouncing and coalescing drops but none of these terms can be used on their own to describe the entire regime. Therefore, the name “composed” arises from the fact that this region is indeed composed of a variety of phenomena including floating, bouncing and coalescing drops. The phenomena found in this regime are formed by low velocity impacts ( $Fr < 30$ ). The first specific flow behaviour encountered is total coalescence. The drops that totally coalesce are characterised by the fact that after impact, they do not give rise to any secondary flow behaviour like jetting or bubble entrapment. In terms of specific behaviour the coalescence cascade, microbubble formation and vortex rings formation can all be observed in this regime. Increasing the impact velocity or Fr number leads to well defined cavity structures. The collapsing cavity can entrap small air bubbles that emit sound and produce high-speed rising jets that break up to produce many secondary drops. This regime of phenomena is referred to as the primary bubble entrapment regime. The secondary drops produced by the jets in this regime return to the free surface with impact conditions that place them in the composed regime.

Increasing the Froude number even further results in changes to the dynamics of cavity collapse and the end of bubble entrapment. This heralds the start of the thick-jet regime or post-entrapment regime as it is called here. The jets in this regime differ greatly to jets in the primary bubble entrapment regime as they tend to be thick slow moving jets that produce single large secondary drops. Also in this regime the crown structure is formed. The thick jets and crown form many secondary drops, which, like the secondary drops formed in the primary bubble entrapment regime, return to the surface with diameters and velocities that place them in the composed regime. In fact one of the only practical ways to produce drops that fall in the composed regime are from the secondary drops formed by the jets in crown in the primary bubble entrapment and post-entrapment jetting regime. At the top end of the post-entrapment regime (*i.e.* when the impact velocity approaches the terminal velocity of the drop), the splash thrown up by the impacting drop closes above the impact site to trap an air bubble on the liquid surface. In practice, there exist many difficulties in producing, controlling and capturing the flow behaviour of drops impacting with such high velocities. Therefore, this particular flow behaviour will not be studied in this thesis.

Before the specific details of all the aforementioned flow behaviour are discussed in 1.5, some theoretical background to the liquid-liquid impact problem needs to be addressed. After the mathematical tools have been described and the specific flow phenomena discussed, this chapter will conclude with a brief discussion on the PIV technique and its use in liquid-liquid impacts along with the objectives of this thesis.

## 1.4 Theoretical Preliminaries

### 1.4.1 Theoretical Flow Description

The governing equations for the liquid-liquid impact problem can be described in terms of the Navier-Stokes equation (1.1) and continuity equation (1.2).

$$\rho \left( \frac{\partial \mathbf{u}}{\partial t} + \mathbf{u} \cdot \nabla \mathbf{u} \right) = -\nabla p + \rho \mathbf{g} + \mu \nabla^2 \mathbf{u} \quad (1.1)$$

$$\nabla \cdot \mathbf{u} = 0 \quad (1.2)$$

Currently, a complete analytical solution to the Navier-Stokes equations is not achievable. In the past many of these mathematical impasses were circumvented with liberal simplifications and assumptions. However, in the case of liquid-liquid impacts the gravitational, viscous and time dependant terms need to be included in the analysis if the equations are to accurately model the physics. Therefore, the Navier-Stokes equations cannot be simplified in this case without losing important physical behaviour.

Further complexity is added to the theoretical description of the problem if surface tension forces at a free surface are included. The surface tension forces arise due to the need for the stresses at the free surface to balance. Here only the normal stresses at the interface are considered (Figure 1.2).

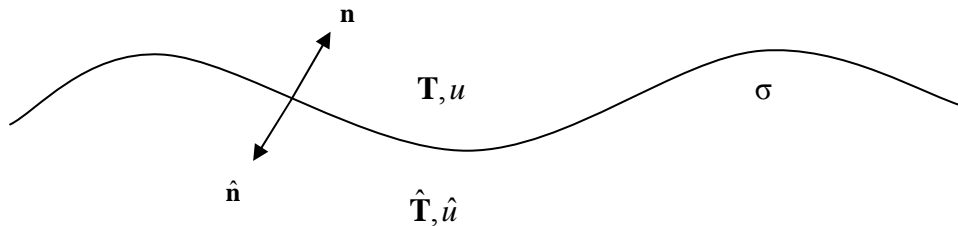


**Figure 1.2** Diagram of the forces acting on an interface. Carats signify properties of the lower fluid

The normal stress condition at the interface can be expressed as

$$\mathbf{n} \cdot \mathbf{T} \cdot \mathbf{n} - \mathbf{n} \cdot \hat{\mathbf{T}} \cdot \mathbf{n} = \sigma(\nabla \cdot \mathbf{n}) \quad (1.3)$$

where  $\mathbf{T} = -p\mathbf{I} + \mu[\nabla\mathbf{u} + (\nabla\mathbf{u})^T]$  is the stress tensor associated with the fluid pressure and velocity. If one of the fluid phases exerts significantly less stress on the interface than the other phase (*i.e.* liquid-gas interface), equation 1.3 further reduces to

$$\mathbf{n} \cdot \mathbf{T} \cdot \mathbf{n} = \sigma(\nabla \cdot \mathbf{n}) \quad (1.4)$$

In short, a complete analytical solution to the equations that govern the liquid-liquid impact problem is currently not possible. Therefore, other techniques such as scaling analysis must be employed to acquire a simplified theoretical understanding of the process and identify the parameters that are important during the process.

#### 1.4.2 Scaling Analysis

Define the characteristic length scale as  $L$ , characteristic velocity scale as  $U$  and reduced pressure as  $p_d = p - \rho gz$ , the following dimensionless variables are formed.

$$\begin{aligned} x^* &= \frac{x}{L}, \quad y^* = \frac{y}{L}, \quad z^* = \frac{z}{L} \\ \nabla^* &= \hat{\mathbf{i}} \frac{\partial}{\partial x^*} + \hat{\mathbf{j}} \frac{\partial}{\partial y^*} + \hat{\mathbf{k}} \frac{\partial}{\partial z^*} = L\nabla \\ t^* &= t \frac{U}{L}, \quad u^* = \frac{u}{U}, \quad p_d^* = \frac{p_d}{\rho U^2} \end{aligned} \quad (1.5)$$

Substituting in the above dimensionless parameters into the Navier-Stokes equation (2.1) results in the following

$$\rho \left( \frac{\partial(\mathbf{u}^* U)}{\partial \left( t^* \frac{L}{U} \right)} + \frac{\mathbf{u}^* U \cdot \nabla^* \mathbf{u}^* U}{L} \right) = - \frac{\nabla^* p_d^* \rho U^2}{L} - \rho g L z^* + \rho g L z^* + \frac{\mu \nabla^{2*} \mathbf{u}^* U}{L^2} \quad (1.6)$$

Grouping like terms and rearranging yields equation (1.7),

$$\frac{\rho U^2}{L} \left( \frac{\partial \mathbf{u}^*}{\partial t^*} + \mathbf{u}^* \cdot \nabla^* \mathbf{u}^* \right) = -\frac{\nabla^* p_d^* \rho U^2}{L} + \frac{\mu \nabla^{2*} \mathbf{u}^* U}{L^2} \quad (1.7)$$

$$\frac{\partial \mathbf{u}^*}{\partial t^*} + \mathbf{u}^* \cdot \nabla^* \mathbf{u}^* = -\nabla^* p_d^* + \frac{\mu}{\rho L U} (\nabla^{2*} \mathbf{u}^*)$$

With the Reynolds number as  $Re = \rho L U / \mu$ , equation 1.8 reduces to

$$\frac{\partial \mathbf{u}^*}{\partial t^*} + \mathbf{u}^* \cdot \nabla^* \mathbf{u}^* = -\nabla^* p_d^* + \frac{1}{Re} (\nabla^{2*} \mathbf{u}^*) \quad (1.8)$$

The dimensionless value  $p_d^*$  is the Euler number. The Froude number normally appears in a scaling analysis of the Navier-Stokes equations but has been shifted into the boundary condition via the use of the dynamic pressure term defined earlier. For completeness the scaling of the continuity equation is shown in equation 1.9 but does not yield any dimensionless parameters of interest.

$$\nabla^* \cdot \mathbf{u}^* = 0 \quad (1.9)$$

The surface tension boundary condition can also be scaled in a similar manner to the Navier-Stokes equations.

$$\mathbf{n} \cdot \mathbf{T}^* \cdot \mathbf{n} = \frac{\sigma}{L} (\nabla^* \cdot \mathbf{n}) \quad (1.10)$$

$$\mathbf{T}^* = -\mathbf{I}(\rho U^2 p_d^* + L \rho g z^*) + \frac{\mu U}{L} (\nabla^* \mathbf{u}^* + (\nabla^* \mathbf{u}^*)^T) \quad (1.11)$$

Combining the above two equation and dividing through by  $\rho U^2$  results in

$$-p_d^* - \frac{Lg}{U^2} z^* + \frac{\mu}{\rho U L} [\mathbf{n} \cdot (\nabla^* \mathbf{u}^* + (\nabla^* \mathbf{u}^*)^T) \cdot \mathbf{n}] = \frac{\sigma}{\rho U^2 L} (\nabla^* \cdot \mathbf{n}) \quad (1.12)$$

Now defining the Froude ( $Fr = U^2 / gL$ ) number and Weber ( $We = \rho L U^2 / \sigma$ ) number yields the final relationship

$$-p_d^* - \frac{1}{Fr} z^* + \frac{1}{Re} \left[ \mathbf{n} \cdot \left( \nabla^* \mathbf{u}^* + (\nabla^* \mathbf{u}^*)^T \right) \cdot \mathbf{n} \right] = \frac{1}{We} (\nabla^* \cdot \mathbf{u}^*) \quad (1.13)$$

Therefore, three key dimensionless groups arise for the scaling analysis, the Froude, Weber and Reynolds number. Thus, all flow phenomena in liquid-liquid impacts can be described with Fr, Re or We numbers or combinations of these numbers.

### 1.4.3 Dimensionless Groups, Length Scales and Time Scales

From equations 1.8 and 1.13 it was shown that the flow is dependant on the several dimensionless groups including the Froude, Weber and Reynolds numbers. These dimensionless numbers essentially describe the relative importance of inertial ( $F_I = \rho U^2 L^2$ ), gravitation ( $F_g = g \rho L^3$ ), viscous ( $F_\mu = \mu U L$ ) and surface tension ( $F_\sigma = \sigma L$ ) forces in the flow.

$$Re = \frac{\rho U L}{\mu} = \frac{Inertia}{Viscosity} \quad (1.14)$$

$$Fr = \frac{U^2}{gL} = \frac{Inertia}{Gravity} \quad (1.15)$$

$$We = \frac{\rho U^2 L}{\sigma} = \frac{Inertia}{Surface Tension} \quad (1.16)$$

The aforementioned forces interact with each other and due to the non-linear characteristics of the Navier-Stokes equation, the relative effects of the forces give rise to other dimensionless quantities depending on the scales the forces operate under. Thus, derived quantities such as the Bond, Capillary and Ohnesorge number can be obtained.

$$Bo = \frac{We}{Fr} = \frac{\rho g L^2}{\sigma} = \frac{Gravity}{Surface Tension} \quad (1.17)$$

$$Ca = \frac{We}{Re} = \frac{\mu U}{\sigma} = \frac{Viscous}{Surface Tension} \quad (1.18)$$

$$Oh = \frac{\sqrt{We}}{Re} = \frac{\mu}{\sqrt{\rho L \sigma}} = \frac{\text{Viscous}}{\sqrt{\text{Surface Tension} * \text{Inertial}}} \quad (1.19)$$

The Bond number describes the relative strength of gravity and surface tension forces. In the case where the gravitational and surface tension forces are similar (*i.e.* Bo = 1) the capillary length scale can be obtained.

$$Bo = 1 = \frac{\rho g L^2}{\sigma} \quad (1.20)$$

$$L = \sqrt{\frac{\sigma}{\rho g}} = l_c$$

If the process occurs with a spatial value approximately equal to  $l_c$ , the phenomena can be said to be affected by both gravitational and surface tension effects. If the spatial value is  $\ll l_c$  surface tension dominates (short distances) and for  $\gg l_c$ , gravity forces dominate (long distances). For water under standard conditions the capillary length scale is 2.73 mm. This method can be extended to derive temporal or spatial scales that describe the relative importance of the competing forces within the flow with respect to each other. For example the time scale for a gravity/inertial driven flow ( $t_g$ ) can be found by using the Froude number.

$$Fr = 1 = \frac{U^2}{gL} = \frac{L^2}{gLt^2} \quad (1.21)$$

$$t = \sqrt{\frac{L}{g}} = t_g$$

The use of dimensionless numbers to examine the relative influence of different forces at different stages of the impact, is the main analysis tool used in this study. Therefore, with the basic theoretical tools now established our attention turns to a review of the specific phenomena that occur in liquid-liquid impacts.

## 1.5 Liquid-liquid Impact on a Deep Pool

### 1.5.1 Total coalescence

The first flow regime examined in this review is the so-called total coalescence regime. In this regime the impacting drops totally coalesce without producing any secondary drops, jets or cavities of any substantial depth. The total coalescing region occurs with drops ranging in size from 20-200  $\mu\text{m}$  and impact velocities  $< 1$  m/s (Cole 2007). These drops are generally formed from other splashing process including, the final stage of the coalescence cascade, secondary drops from the thin high-speed jets, secondary drops from crown formation or from the break-up of the jets that results from an air bubble bursting at the free surface. Research in this area has been hampered because these small drops cannot be easily formed from a controlled process (*i.e.* pinch off from a needle).

Thoroddsen and Takehara (2000) investigated the total coalescence regime while investigating the forces that prevent the coalescence cascade (see section 1.5.2) from continuing indefinitely. Thoroddsen and Takehara (2000) suggest that viscous forces prevent partial coalescence, as experienced in the coalescence cascade, by damping out the capillary waves that act to deform the drop to form a child drop. Furthermore, Thoroddsen and Takehara (2000) suggest that a Reynolds number limit of 20, based on drop size, may signal the transition between total and partial coalescence. However, no evidence in their paper is shown to support this argument. More recently Aryafar and Kavehpour 2006 have made further attempts to provide a limit on the total coalescence process using the Ohnesorge number rather than the Reynolds number. Their results suggest an Ohnesorge number  $> 1$  will lead to total coalescence while a Ohnesorge number  $< 1$  leads to partial coalescence. Since the Oh number is defined as  $Oh = \mu / \sqrt{\rho L \sigma}$ , an Oh number  $> 1$  indicates that the viscous forces are dominating over surface tension and inertial forces. This is consistent with the arguments made by Thoroddsen and Takehara (2000). A more through review of this area can be found in Neitzel and Dell'Aversana 2002.

### 1.5.2 Coalescence Cascade

The coalescence cascade is one of the more fascinating processes that occur during liquid-liquid impacts and has been reported by numerous authors (Charles and Mason (1960); Pikhitsa and Tsargorodskaya (2000); Thoroddsen and Takehara (2000); Liow (2001); Honey and Kavehpour (2006)). The coalescence cascade has been identified as a repeating, self-similar, partial coalescence process. An image sequence of the cascade is shown in Figure 1.3. In Figure 1.3 a drop impacts on the liquid surface before rebounding and coming to rest on the surface in the frame labelled 116 ms. At this stage an air film must separate the two liquid bodies. The film separating the drop and pool drains or ruptures with the passage of time and allows the two liquids to come into contact. Moments after this has occurred, the unbalanced surface tension forces trigger a capillary wave that travels up the drop (120 ms) and distorts its shape causing a child drop to be pinched off (123 ms). The child drop accelerates towards the surface, bounces and comes to rest just as its parent drop did. After a short period, the air separating the two liquid bodies again drains allowing the process to repeat. A stage is used to describe the time from when one drop separates and comes to rest on the surface then partially coalesces to form another smaller drop.

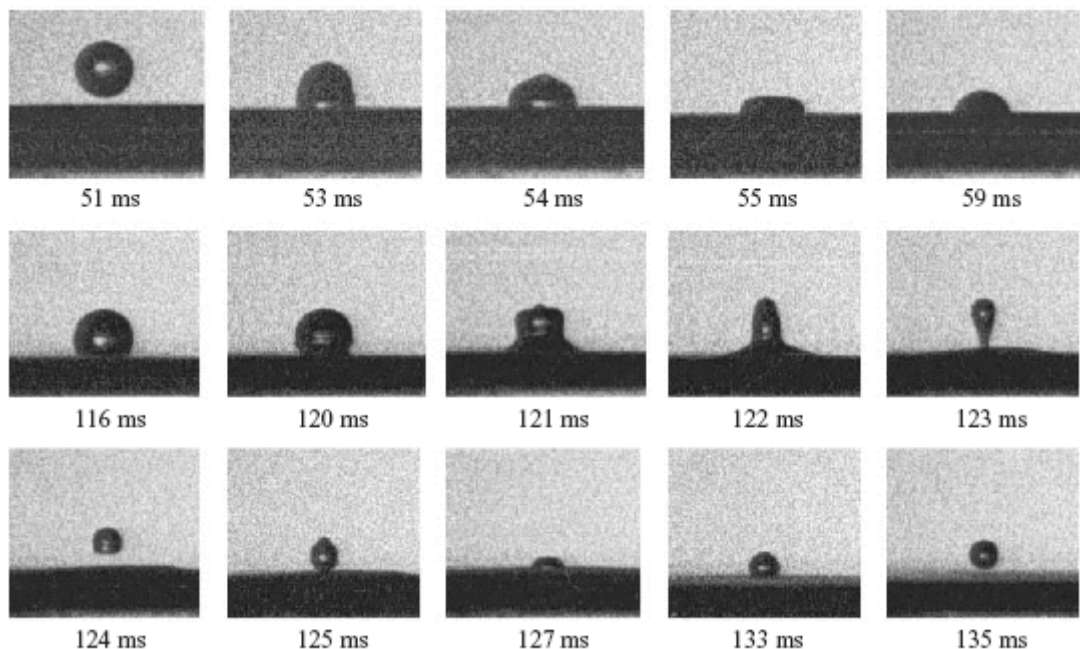


**Figure 1.3** The coalescence cascade (Liow 2001)

Analytical solutions to the coalescence cascade have been pursued with some success. Thoroddsen and Takehara (2000) suggested a capillary time scale for the process based on a balance between surface tension and inertial forces (equation (1.22)).

$$\tau = \sqrt{\rho D^3 / \sigma} \quad (1.22)$$

Their experimental data confirms that  $\tau \propto D^{3/2}$  does indeed hold for the coalescence cascade process. Another observation by Thoroddsen and Takehara (2000) observed that the following stage in the cascade will always rise higher than the previous. However, Honey and Kavehpour (2006) included a trace of the drops in the cascade that contradicted this (Figure 1.4). In Figure 1.4 the second drop in the cascade does not rise higher than the first stage of the process but the third, fourth and fifth do jump higher than second drop. Honey and Kavehpour (2006) constructed a model based on a dynamic balance between gravitational forces and surface tension forces rather than surface tension/inertia. However, Honey and Kavehpour (2006) did use the capillary time scale in equation (1.22). The result of their model is quite lengthy and is shown in equation 1.23.  $R_1$  is the radius of the first drop in a stage.  $R_2$  is the secondary drop formed at the end of a stage.  $A$  is the coefficient of restitution for the bouncing.  $V_i$  is the impact velocity,  $V_b$  is the bouncing velocity.  $r_i$  is the ratio of drop diameter.  $A = V_b / V_i = \sqrt{4gR_1 + V_0^2} / \sqrt{2gh_{\max}}$ .  $r_i = R_2 / R_1$  and  $V_0 = e^{-1} \sqrt{3\sigma / 2\rho r_i^3 R_1} + g\sqrt{\rho R_1 / \sigma}$

$$\frac{h_{\max}^*}{A^2} = \frac{3}{4e^2 r_i^2 R_1^*} + R_1^* \left[ 2 + \sqrt{\frac{3}{2e^2 r_i^3}} \right] + \frac{R_1^*}{2} \quad (1.23)$$

Equation 1.23 estimates the jump height the drop formed during the coalesce cascade based on the size of the secondary drop formed and initial drop size. A plot showing a comparison between their analytical model to experimental data is shown in Figure 1.5.

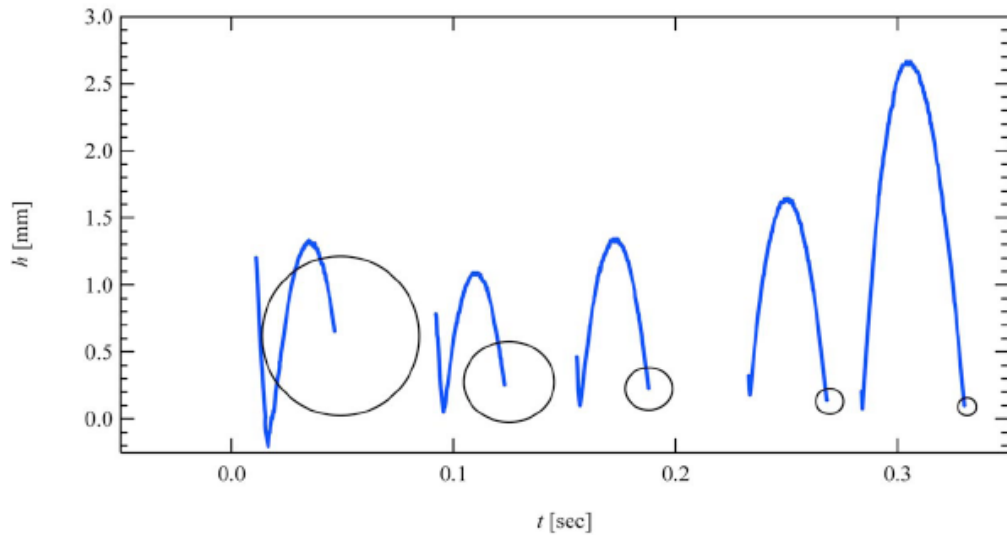


**Figure 1.4** Trajectory trace of drops in the coalescence cascade (Honey and Kavehpour 2006)

The correlation is quite close but most importantly it predicts that the second drop in the process will not jump as high as the first or third drops in the process. Thus, the coalescence cascade can be described as a surface tension/gravity governed process. In the later stages of the coalescence cascade the drop sizes become very small. At the smaller length scales viscous forces become increasingly important and will dominate the process to prevent secondary drop formation, allowing total coalescence to occur. While it may appear many of the questions regarding the coalescence cascade have been answered many questions still remain including how the air film between the two liquid bodies actually forms, the forces that drive the drainage of the film, and if the film ruptures to leave air bubbles entrapped in the bulk fluid.

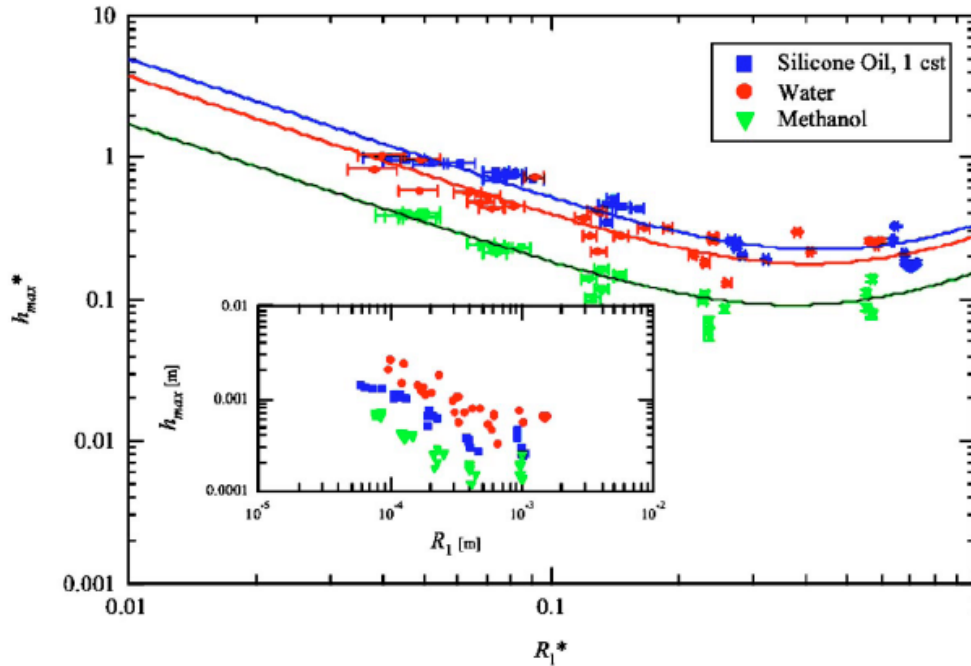


**Figure 1.5** Comparison between analytical model and experimental results for the coalescence cascade  $h_{\max}^*$  being the maximum height obtained during each stage (normalised by capillary length) and  $R_1^*$  the drop radius (normalised by capillary length). Minimum jump height is achieved at approximately  $R_1^* = 0.4$  (Honey and Kavehpour 2006)

### 1.5.3 Air film formation and rupture

For some time it has been known that under certain circumstances the impact of a liquid drop can leave many microbubbles entrapped in the bulk fluid (Blanchard and Woodcock 1957). Esmailzadeh and Mesler (1985) provided the first spectacular series of images showing how many hundred, possibly thousands, of microbubbles ( $< 200 \mu\text{m}$ ) were being formed after the impact of a liquid drop. Furthermore, the bubbles were being transported deep into the fluid by a vortex ring. Further investigation by Sigler and Mesler (1990) showed that the origin of the bubbles is from the destruction of a thin air film between the drop and surface (Figure 1.6). The expanding cavity stretches the gaseous film until it reaches an unstable thickness and ruptures.

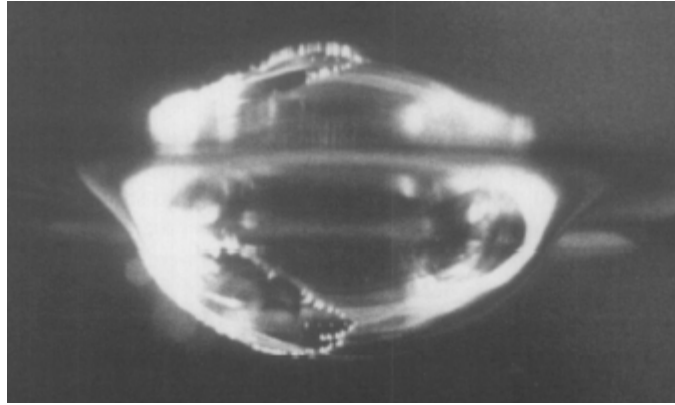


**Figure 1.6** Rupturing of the air film between (Sigler and Mesler 1990)

In both of these papers the impacting drops ranged in size from 2.6 mm to 4.4 mm falling from heights of 10 mm to 30 mm. However, both of these studies were hampered by inadequate imaging equipment. They could not continuously record the rupture process so they had to rely on compiling images from different impacts to build up a picture of the phenomena. One interesting point to note is that when the actual rupture of the film was captured like in Figure 1.6 the bubbles formed were quite large. However, in cases where the rupture occurred too quickly to even be captured with freeze frame shots, the bubbles were far smaller in size. Therefore, it appears that the bubble size resulting from a film breakup is dependant on the rupture velocity.

Recent work by Thoroddsen *et al.* (2003) using a high speed camera has shed more light on the breakup of thin films in liquid-liquid impacts. Again like the previous authors, Thoroddsen *et al.* (2003) could only detect the formation of microbubbles at low Weber number impacts ( $We < 22$ ). Interestingly Thoroddsen *et al.* (2003) observed the rupture of the gaseous film at very different stages of cavity development (Figure 1.7). On the left side of Figure 1.7 the thin film ruptures quite early in the cavity formation process to produce thousands of microbubbles. In the right side of Figure 1.7 the air lined cavity breaks up after the cavity has expanded significantly and produces less than 100 larger bubbles. The air films appear to originate from an air film entrapped as the drop and pool fluid coalesce but no explanation has been provided for how this film becomes entrapped or any upper or lower limits on this phenomena.

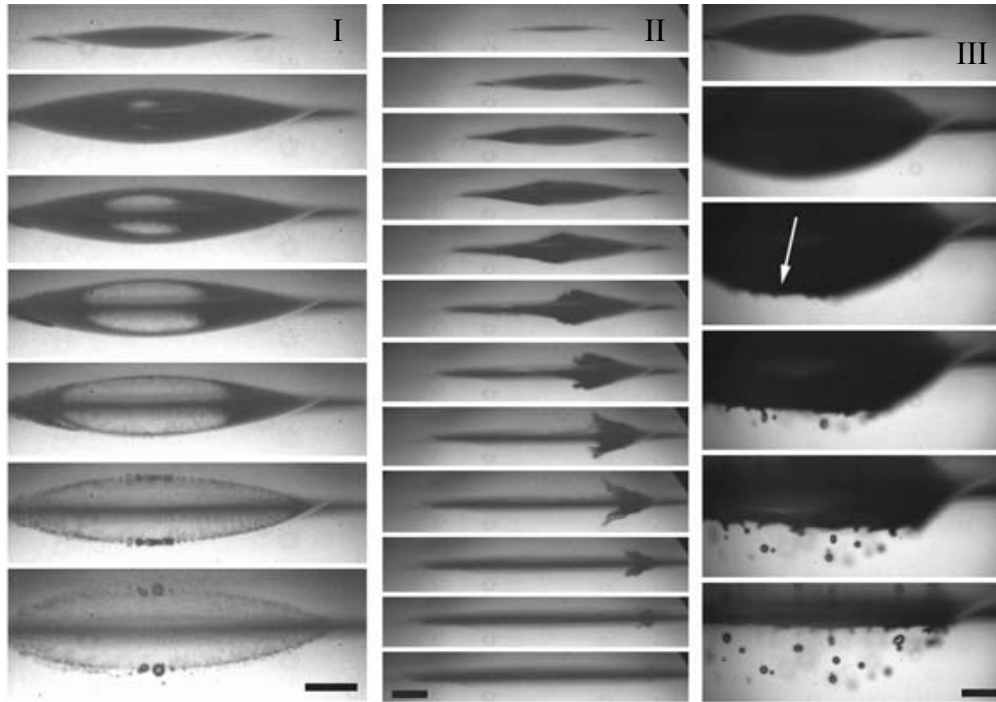


**Figure 1.7** Thin film rupture at different stages of cavity development for three different impacts (Thoroddsen *et al.* 2003)

#### 1.5.4 Thoroddsen bubbles

Several researches have reported the formation of one or two small bubbles (50  $\mu\text{m}$ ) to propagate ahead of the growing cavity (Blanchard and Woodcock 1957; Peck and Sigurdson 1994). The exact origin of these tiny bubbles was unknown. Using advanced digital cameras (1 million FPS @ 260x312), (Thoroddsen *et al.* 2003) have captured the formation of these bubbles. They identified that between Weber numbers 14 and 282, a thin air sheet is formed between the impacting drop and liquid surface. This air sheet rapidly contracts due to surface tension, to produce an unstable necklace structure, which in turn collapses to produce one or two small bubbles (Figure 1.8). The whole event occurs in less than 1 ms. In this study the bubbles formed by this mechanism will be called Thoroddsen bubbles. Thoroddsen *et al.* (2003) found that the thickness of the air sheet was approximately inversely proportional to impact velocity for higher velocity impacts (i.e. the sheet thickness decreased with increasing impact velocity). At lower velocity impacts, where the drop was still oscillating as it impacted, the radius of curvature of the drop was found to have a strong bearing on the sheet thickness. Thoroddsen *et al.* (2003) derived an expression that predicts an exponential reduction of the sheet radius with time (Equation 1.24). This solution is based on previous

observations on the contraction speed of air sheets by Oguz and Prosperetti (1989) and an assumption that the volume of the air sheet is constant during the contraction event.

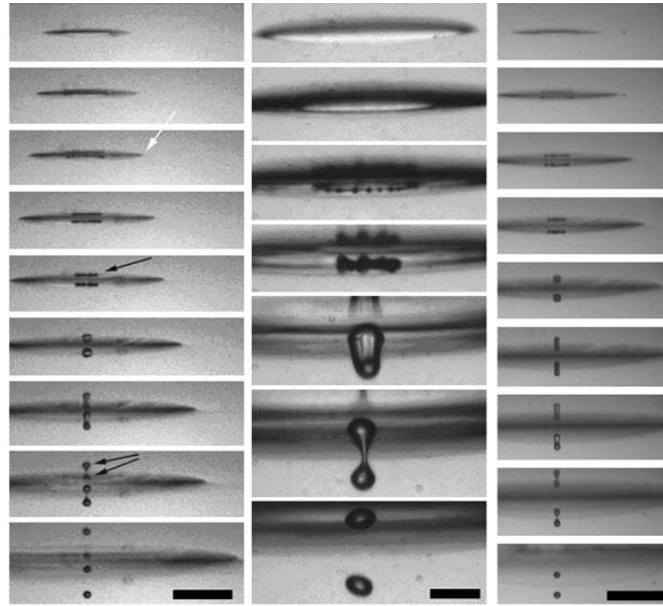


**Figure 1.8** Formation of Thoroddsen Bubbles via air sheet contraction (Thoroddsen *et al.* 2003)

$$r_s(t) = r_{s,0} e^{(-C\sqrt{\pi\sigma/(\rho_{pool}V_s)}t)} \quad (1.24)$$

The above relationship was confirmed with experimental observations over several different impact velocities. The outcomes of their analysis suggest that the contraction event is based on a balance between surface tension and inertial forces while viscous forces are not significant. However, Thoroddsen *et al.* (2003) provide no insight or explanation into the actual origin of the air sheet.

### 1.5.5 Oguz-Prosperetti bubble rings

Another microbubble feature observed by Thoroddsen *et al.* (2003) was a fine ring of extremely small bubbles (25  $\mu\text{m}$ ) propagating ahead of the two Thoroddsen bubbles. This ring of bubbles is believed to be the first experimental evidence of Oguz-Prosperetti bubble rings. The formation of such structures were first predicted by the liquid bridge numerical simulations of Oguz and Prosperetti (1989). In this study Oguz and Prosperetti (1989) closely investigated the region where two liquid bodies contact each other. They showed that surface tension effects can distort the surfaces of the two

bodies inducing an uneven contact. This uneven contact allows a toroidal pocket of air to become entrapped between the two bodies. It has been postulated that this toroidal pocket of air would rapidly expand and breakup forming a series of microbubbles. This is a different form of bubble entrapment to the thin film rupture discussed in 1.5.3 but may share some similarities with the formation of Thoroddsen bubbles.

### 1.5.6 Cratering dynamics

In most liquid-liquid impacts, a cavity or crater will be formed in the target media due to the high energy of the impact. The dynamics of how the cavity forms and collapses gives rise to much of the phenomena found in the field of liquid-liquid impacts. The formation and collapse of the cavity has been observed to undergo several stages of development. Initially, the cavity expands radially out from the impact site. The exact shape of the expanding cavity depends on impact velocity and drop eccentricity. When the kinetic energy of the expanding cavity have been converted to potential energy, the heavier surrounding fluid acts to collapse the cavity. Depending on how the cavity collapses several different secondary events can occur including jetting and bubble entrapment.

Some of the early work on liquid-liquid impact cratering comes from Engel (1966, 1967) who performed both analytical and experimental research. Engel (1966, 1967) studied the impact of drops falling at terminal velocity. Comparing the potential energy of the drop to the surface energy and potential energy of the cavity, a solution for the maximum cavity radius was formulated, assuming a hemi-spherical expansion. However, the resulting equation is quite lengthy and specific to drop close to terminal velocity. Pumphrey and Elmore (1990) attempted to simplify the maximum cavity equation neglecting the wave swell and secondary drops that may be formed on impact. Pumphrey and Elmore (1990) equated the kinetic energy of the impacting drop to the potential energy of a hemi-spherical cavity giving the following relation.

$$R_m^* = \left( \frac{Fr}{3} \right)^{\frac{1}{4}} \quad (1.25)$$

Pumphrey and Elmore (1990) showed experimental results that conformed to the  $R_m^* \propto Fr^{\frac{1}{4}}$  scaling. However, the coefficient of the relationship was not quite correct. Liow (2001) performed a least squares fit on the data and modified the proportional constant to take into account that not all the kinetic energy of the drop is converted into potential energy of the cavity.

$$R_m^* = 0.727 \left( \frac{Fr}{3} \right)^{\frac{1}{4}} \quad (1.26)$$

It should be noted that all the above scaling is based on the potential energy of a hemi-spherical crater. This assumption is valid for high velocity impacts. However, at lower impact velocities the hemi-spherical expansion assumption breaks down as surface tension effects begin to dominate and distort the interface. Thus, there is scope for a more detailed understanding of the cavity formation dynamics at lower impact velocities.

### 1.5.7 Vortex Rings

The formation of toroidal structures or vortex rings from liquid-liquid impact has been the subject of many studies for over a hundred years (Thomson 1885). Vortex rings are extremely important as they are the primary mechanism for moving the microbubbles created during initial stages of impact deep into the bulk fluid so that oxygen exchange can occur (Durst 1996). Vortex rings generally appear at low velocities with Weber and Froude numbers in the order of 20 – 50. Experimental studies of vortex rings have involved observing the formation of vortex ring structures by adding a visual tracer to the impacting drop. Vortex rings appear after the drop has coalesced with the bulk liquid and the cavity has retracted where the dyed tracer fluid collects into the vortex ring structure. A vortex ring can be described as fluid spinning around a circle enclosed by a toroid (Figure 1.9). The vortex ring travels downward and expands, radially.

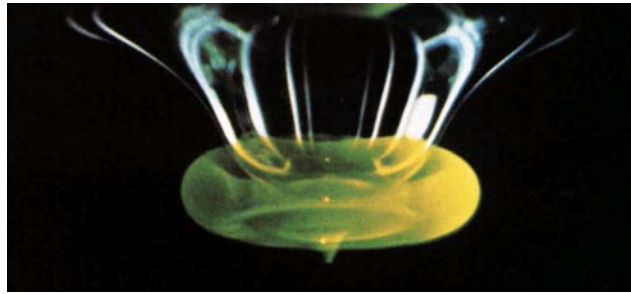


**Figure 1.9** Vortex ring formed by a 2.8mm drop falling 38.4 mm (Peck and Sigurdson 1994)

In Thomson (1885) early experiments he observed that the penetration depth of the vortex ring varied with release height but could not explain why. Chapman and Critchlow (1967) went on to show that the penetration depth is related to the oscillation phase of the drop as it hit the surface Figure 1.10. Examining Figure 1.10 the optimal shape for maximum penetration is occurs when the drops are spherical or near spherical. When the drop is prolate or oblate, vortex ring penetration is significantly inhibited. However a study by Rodriguez and Mesler (1987) suggested that maximum penetration was achieved when the impacting drop was prolate in shape while the minimum penetration corresponded to a oblate drop shape. Their rationale for explaining this contradiction was related to the way cavity forms and collapses. Oblate drops produce very different cavity shapes to prolate and spherical drops. Therefore, describing the optimal penetration depth in terms of release height may be oversimplifying the problem. It is more likely that several factors including drop phase, drop size and surface tension all contribute to influence the cavity shape and thus vortex ring formation. However, this has not been described in any literature to date. Attempts have also been made to track the diameter and penetration depth over time to gain more insight into how the vortex ring forms and evolves. Durst (1996) conducted a detailed study on the evolution of the vortex ring over time and suggested there exists different regions of vortex ring development (Figure 1.11).

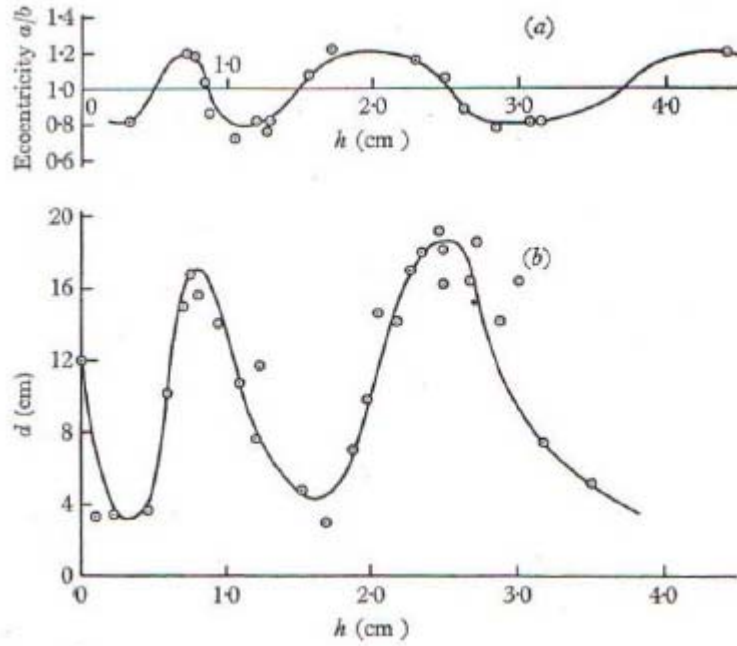


**Figure 1.10** Relationship between drop eccentricity and vortex ring penetration depth (Chapman and Critchlow 1967)

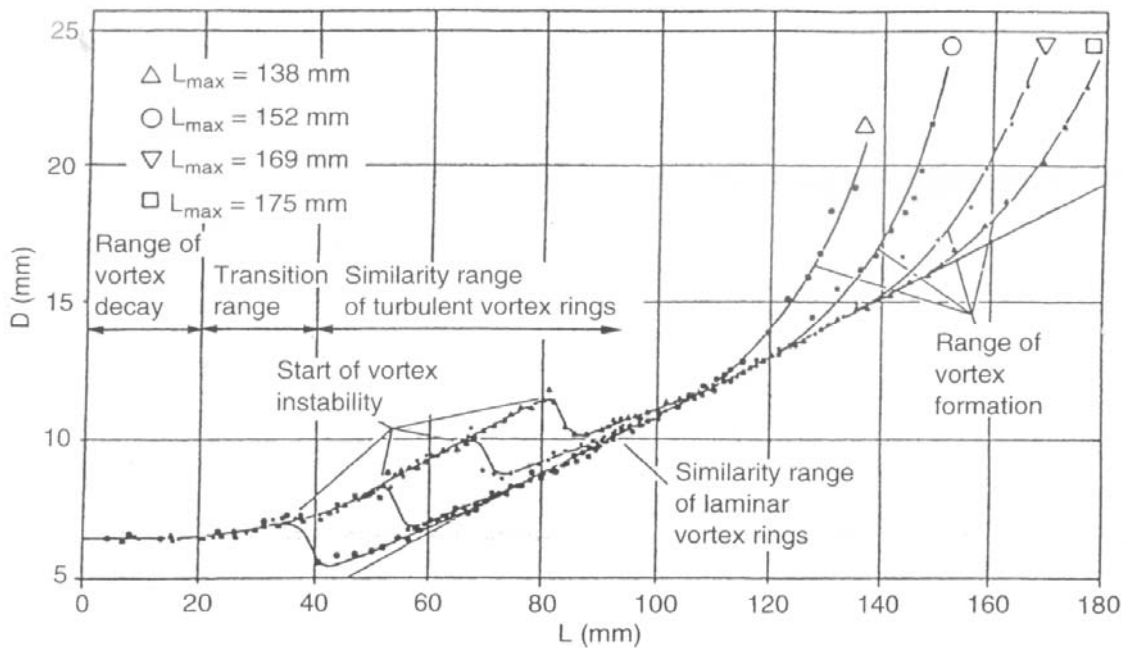


**Figure 1.11** Vortex ring diameter ( $D$ ) as a function of penetration depth ( $L$ ) (Durst 1996)

Initially the vortex ring diameter is constant over time as it develops. The vortex ring then enters a region a laminar region  $D \propto \sqrt{t}$ . The vortex ring then becomes unstable and transits into a turbulent region. In the turbulent region the scaling of the diameter with time is given by  $D \propto \sqrt[3]{t}$ . Peck and Sigurdson (1995) also examined the evolution

of the vortex ring and suggest a time scale of  $t = \frac{D}{2} U^{1/3} c^{-4/3}$ , where  $c$  is the capillary wave speed.

While the evolution and development of the vortex ring have been studied widely, the exact mechanism that gives rise to the vortex ring is still the source of much debate. Thomson (1885) initially described the formation of a vortex ring as a sheet of vorticity that is formed during the initial contact of the drop and liquid surface. The drop now being squashed into a disk shape will evolve into a vortex ring if the viscosity allows the vorticity to diffuse at the edges of the drop. Peck and Sigurdson (1994) proposed a similar mechanism where the vorticity generated during impact between the drop and pool in the form of a vortex sheet, rolls up to form the vortex ring. Chapman and Critchlow (1967) suggest that surface tension is important in the vortex ring formation process. They claim the vortex ring is the result of high curvature at the point of contact generating a pressure gradient. This gradient then drives a circulatory motion that leads to the formation of a vortex ring. They also suggest that the internal circulation of the drop due to oscillations would assist in driving the pressure gradient. Cresswell and Morton (1995) presented arguments that the vortex rings are the result of boundary layer development and separation. The velocity gradients generated during this process provide the vorticity necessary to generate the vortex rings. However, only limited experimental evidence was presented in their article to support their arguments. Thus, a satisfactory answer cannot be found unless more pertinent information about the flow field around the vortex is gathered.

### **1.5.8 Jets without bubbles**

For many years, it was thought that the thin jet formation was independent of any other phenomena during the splashing event. This argument changed when Rein (1996) suggested that the appearance of the thin jet as a necessary by product of bubble entrapment. However, Liow (2001) observations suggest that jets can occur in a small region just prior to bubble entrapment (Figure 1.12).

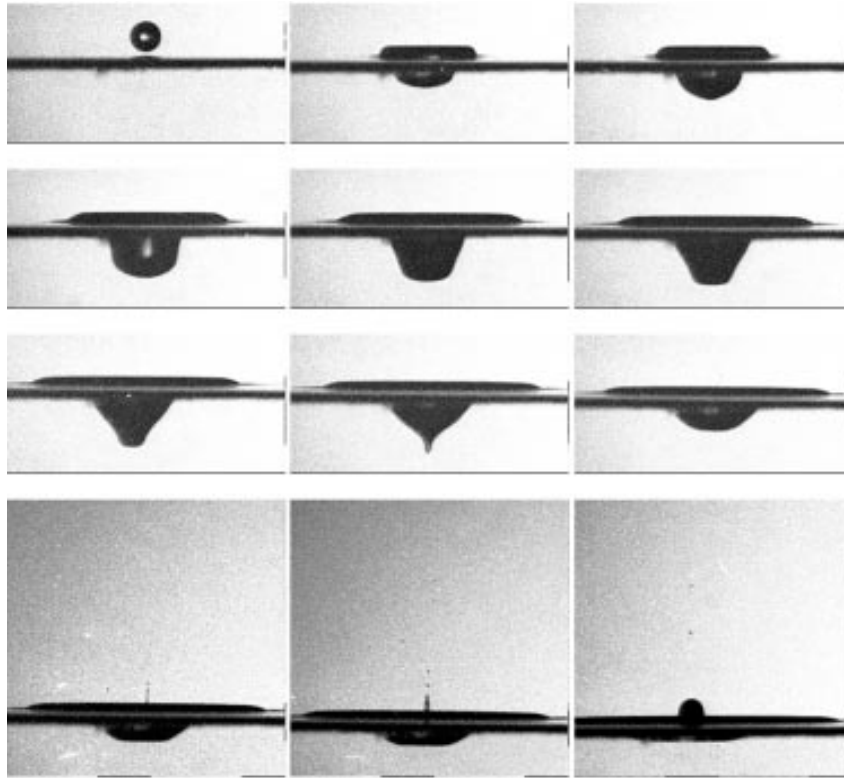


**Figure 1.12** Thin high-speed jet with no bubble entrapment (Liow 2001)

Liow (2001) did suggest that the possible origin of these jets may be an extremely small bubble being entrapped that escaped detection. However, even after increasing the resolution to  $10\ \mu\text{m}$ , no bubbles could be detected. Inferring that bubble entrapment is not a requirement of high speed jetting, this is in conflict with the data of Rein (1996). Liow (2001) had insufficient data to draw any firm conclusions about the bounds of this region of pre-entrapment jetting. Therefore, the validity of any high speed jetting with bubble entrapment needs to be investigated more thoroughly. Furthermore, if this region does indeed exist the underlying mechanics driving the process need to be understood.

### **1.5.9 Primary bubble entrapment and thin jets**

Liquid-liquid impacts have been known to emit audible sound. One of the early researchers to investigate this area was Franz (1959). Franz found that a contributing factor to the sound emitted from an impact was due to an air bubble being trapped under the surface. However, Franz postulated that the entrapment of a bubble was a random event and only played a minor role in sound generation. Pumphrey and Elmore (1990) work involved synchronising a hydrophone with high speed images to highlight the

stages of the impact that produced the strongest acoustic impulse. They showed that the bubble entrapped from the cavity collapse oscillates at audible frequencies and is the dominant source of sound from liquid-liquid impacts. Oguz and Prosperetti (1990) further extended this work by firmly defining the region, in terms of a Weber-Froude number relationship where primary bubble entrapment would occur. Oguz and Prosperetti (1990) suggested a relation of  $We \propto Fr^{1/4}$  for the upper limit and a lower limit of  $We \propto Fr^{1/5}$  for bubble entrapment. Good correlation between these limits and the experimental data was shown by Oguz and Prosperetti (1990).

The predictable nature of the phenomena led it to be called “regular entrainment”. Morton *et al.* (2000) went on to describe the resulting bubble entrapment and thin jet as the result of capillary waves propagating through the cavity causing the collapsing walls to come together. Recent work into the dynamics of the crater formation and collapse by Liow (2001) has shown that a segment of the profile of the cavity prior to collapse, for high speed waves, conforms to an analytical solution for the Crapper wave (Figure 1.13), a nonlinear capillary wave. The jagged line in the figure is a pixel outline of the cavity. However, the Crapper wave solution only fits the initial portion of the cavity and breaks down prior to jet formation due to a singularity.

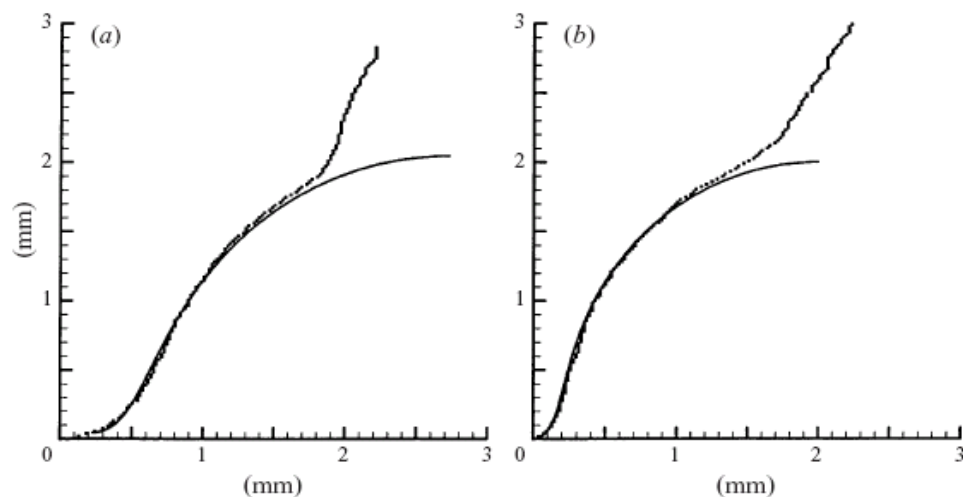


**Figure 1.13** Pixel outline of cavity with solution to Crapper wave (Liow 2001)

Hallett and Christensen (1984) observed another interesting event during cavity collapse from analysing high-speed photographs. The presence of a thin high-speed jet from the base of the cavity was observed. Thin jets were observed to rise at speeds several times the impact speed and spray a fine mist out of the cavity. The thin jets were believed to

occur independent of any other phenomena.. However, Rein (1996) for the first time made the connection between these two different phenomena. The thin jets only occurred after an air bubble had been entrapped under the liquid surface. Rein (1996) put forward the argument that as the cavity walls approach the centreline of the cavity the radial motion must be accompanied by an axial motion to conserve mass. This results in the high-speed jet forming with capillary instabilities causing the rising jet to break-up into many small droplets. Thin jets are formed from so called radial focusing, which is a cumulative effect from the walls accelerating inwards. The exact forces that leads to the walls accelerating inward have still not be adequately described.

Rein (1996) also showed an interesting phenomena in where it appeared the entrapped bubble splits into two smaller bubbles almost immediately after snap off. Rein (1996) attributed this effect to an asymmetric cavity collapse. However, Elmore *et al.* (2001) experimentally showed evidence of the bottom of the cavity breaking up to form multiple small bubbles. These bubbles were not in the same order of size as the bubbles reported by Rein (1996). However, the bubbles were formed in a similar manner. The shape of the cavity base just before breakup is also very similar to numerical simulations conducted by Oguz and Prosperetti (1991), thus making it quite possible that a zone of multiple primary bubble entrapment may occur but need to be properly delineated.

#### 1.5.10 Downward Jets

In dyed drop experiments, both Elmore *et al.* (2001) and Rein (1996) have both reported the apparent presence of a downward jet accompanying the upward jet during bubble entrapment (Figure 1.14). A downward jet being one that travels away from the free surface, vertically downward into the bulk fluid.

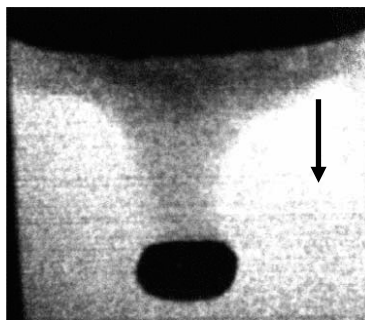


**Figure 1.14** The downward jet associated with bubble entrapment (Elmore *et al.* 2001). Arrow indicates the “downwards” direction of the jet

Rein (1996) postulated that the downward jet is a necessary by-product of radial flow focusing due to the need for momentum to be conserved. This jetting associated with bubble entrapment is somewhat similar to the Munroe effect that causes high-velocity jetting (in both directions) in shaped charges. A shaped charge is a conical object, (that is lined with explosives and metal) analogous to the splash cavity. The detonation of the explosive causes the metal lining to accelerate inward rapidly. When the opposing metal linings contact along the centre line, the material is driven axially in both directions in the form of jets. Birkhoff *et al.* (1948) has modelled this process using a conservation of momentum principal for incompressible fluids to show one would expect a jet in both directions to occur. Fedorchenko and Wang (2004) attempted a similar analysis using the hydrodynamic theory of cumulative jets to analyse the problem. The outcome of their analysis is shown in Figure 1.15. While some circumstantial evidence that downward jets exist (*i.e.* Figure 1.14) have been presented, any clear evidence of the downward jet is yet to be presented. Furthermore, the upward and downward jet velocities described in Figure 1.15 have yet to be verified.

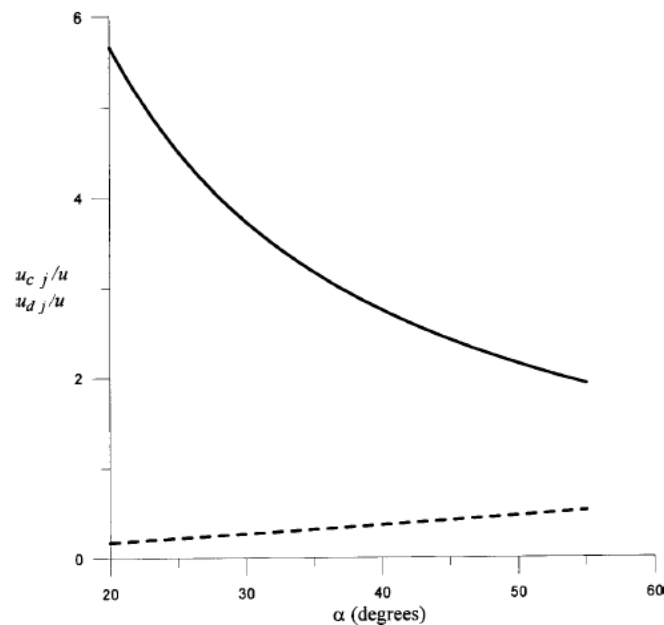


**Figure 1.15** Relationship between upward and downward jet velocity (Fedorchenko and Wang 2004)

### 1.5.11 Crown formation

One of the most spectacular phenomenon in liquid-liquid impacts originally identified by Worthington (1908) is the formation of the crown (Figure 1.16). The crown is the result of a thin fluid sheet rising around the impact zone of the drop that rapidly breaks

up to form a series of secondary drops. Extensive work has been conducted on the formation of the crown for thin films (Davidson 1998; Weiss and Yarin 1999; Roisman and Tropea 2002; Sivakumar and Tropea 2002; Rioboo *et al.* 2003). While the pool depth has been shown to change the height to which the crown will rise (Cossali *et al.* 2004) the forces that are responsible for its formation and breakup remain the same for both deep pools and thin films. Rieber and Frohn (1993) has shown that the actual break-up of the thin film is the result of surface tension driven instabilities. The origin of the crown and the forces that control its formation has also been explored. Engel (1955) postulated that the formation of the crown was due to a pressure wave created at impact. However, numerical simulations by Weiss and Yarin (1999) has highlighted the formation of a small jet emanating from the “neck” region where the contact between an impacting liquid drop and liquid pool occurs (Figure 1.17). Their numerical formulation was based on a surface tension and gravity model while viscosity and compressibility were neglected. The outcomes of these numerical simulations suggest a jet or more correctly an ejecta sheet, due to the axi-symmetric nature of the contact, will form at the “neck” region. This inertially dominated sheet continues to expand outward to form the crown structure a short period later.

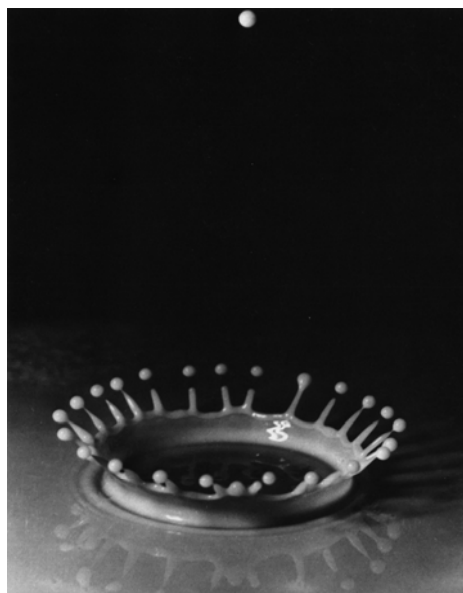


**Figure 1.16** Crown formation due in milk (Edgerton and Killian 1979)

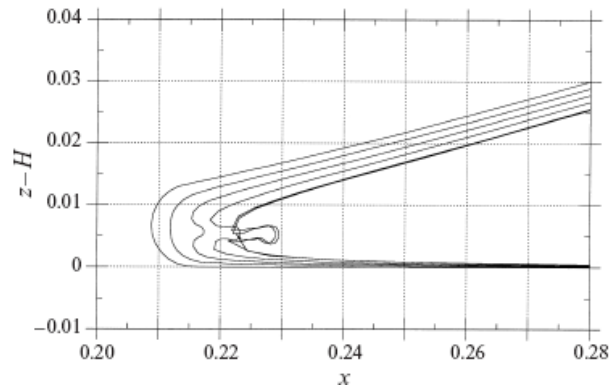


**Figure 1.17** Numerical simulations showing the formation of a high speed jet or ejecta sheet at the drop-pool interface during initial impact (Weiss and Yarin 1999)

No physical evidence of this jet had been observed until Thoroddsen (2002) carried out a study of the ejecta sheet using a Nd:YAG laser with Fluorescein dyed water droplets and pool fluids (Figure 1.18). The outcomes of this study suggest that the origin of the ejecta sheet is from the bulk fluid not the drop itself. The ejecta sheet was tracked to be emanating at 62 m/s, a value over 13 times the impact velocity. The ejecta sheet itself was measured to be moving slight slower at 48 m/s, which corresponds to approximately 10 times the impact velocity. The ejecta sheet initially travels parallel to the bulk fluid surface and is dominated by inertial forces. Shortly after the birth of the ejecta sheet, surface tension forces begin to dominate and the sheet begins to curl downwards towards the free surface. The speed of the sheet now dramatically decelerates to approximately 2.5 m/s after 1 ms, owing to higher viscous forces but continues to grow radially outward with time to form a crown structure. Thoroddsen went on to show that the process is viscosity dependant and this was the primary reason the shapes described by Weiss and Yarin (1999) numerical simulations are very different to what was observed physically.

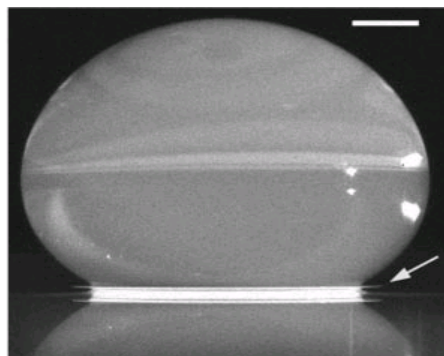


**Figure 1.18** Ejecta sheet from impact (Thoroddsen 2002)

While understanding for the forces that are driving the crown formation process has had some success, acquiring satisfactory criteria for the onset of crown formation has not been obtained. Numerous authors have presented results of splashing occurring with  $We$  numbers ranging from 40 to over 1000. Other authors have shown no crown formation within this zone. From a qualitative perspective the formation of the crown in deep pool impacts has only been shown to occur past the primary bubble entrapment regime (Rein 1993; Liow 2001). Since the upper boundary of the primary bubble entrapment regime is bound by a  $Fr$ - $We$  number relationship it then follows that the formation of the crown must follow a similar relationship. Thus, the crown formation is not solely dependant on  $We$  number but dependant on the  $Fr$  number as well. However, where this boundary lies is not clear cut. Liow (2001) has also shown that the formation of the crown does not occur spontaneously after some limit (*i.e.*  $Fr$ - $We$  number) has been exceeded. Rather there exists a transitionary zone when the crown only partially forms (Image sequence B in Figure 1.19). The exact mechanics of why this partial crown forms is not clear.

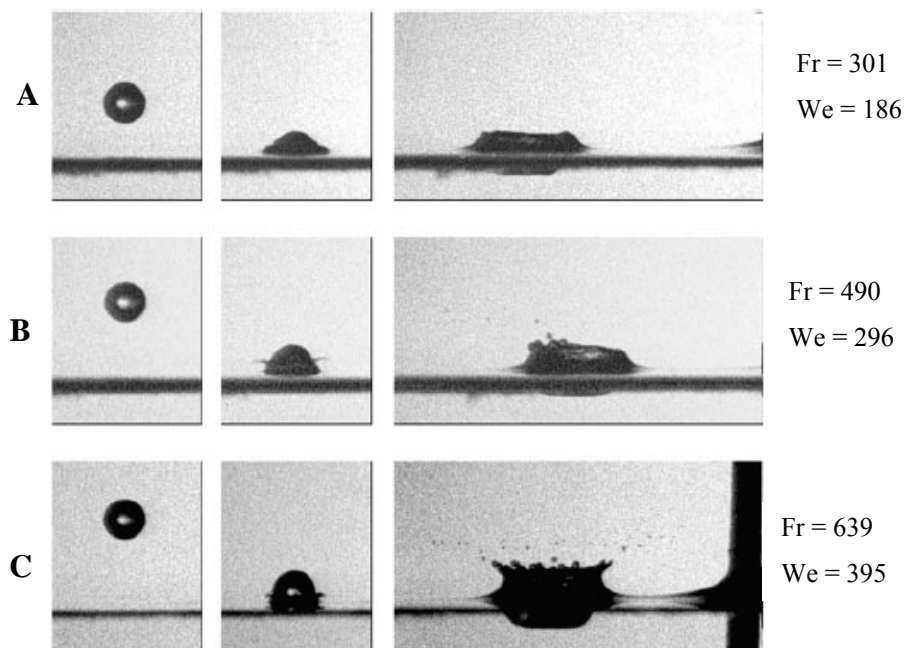


**Figure 1.19** Development of crown formation: (A) No crown formation (B) Partial crown formation (C) Fully developed crown formation (Liow 2001)

### 1.5.12 Thick Jets

One of the many features of splashing identified by Worthington (1908) was the formation of a thick jet that formed after the collapse of the cavity. This structure often

called the Worthington jet is the result of the cavity collapsing at high impact velocities. The thick jet rises above the free surface and usually breaks up into one or more secondary drops (Rein 1996) (Figure 1.21). These secondary drops, depending on their size and height at break off, can return to the free surface and initiate many of the phenomena observed in the composed regime. Furthermore, the appearance of the thick jet is a signal that primary bubble entrapment is no longer occurring and a shift in cavity collapse dynamics has occurred. Although this phenomena has been known for over 100 years, it is, surprising then that very little work has been conducted on understanding how the jet grows and develops. Moreover, there has been no study on the shape or structure of the jet and the forces influencing its development. Some of the only quantitative data on the height development of the jet with increasing Froude number comes from Liow (2001) while Fedorchenko and Wang (2004) have attempted to model the thick jet formation. Here Fedorchenko and Wang (2004) assume the shape of the jet to be a circular cylinder and determine the height and diameter of the jet based on an energy balance. The outcomes of there model suggest a height and diameter scale  $\propto Fr^{1/4}$ . Data published in their article seem to exactly match their scaling (Figure 1.20) but the lack of data presented does not confirm the validity of the scaling. It must be pointed out that the development of the thick jet in water liquid-liquid impacts exhibits a more conical shape rather than a cylindrical one (see Rein 1996). Furthermore, no evidence was presented to support the diameter scaling being  $\propto Fr^{1/2}$ .

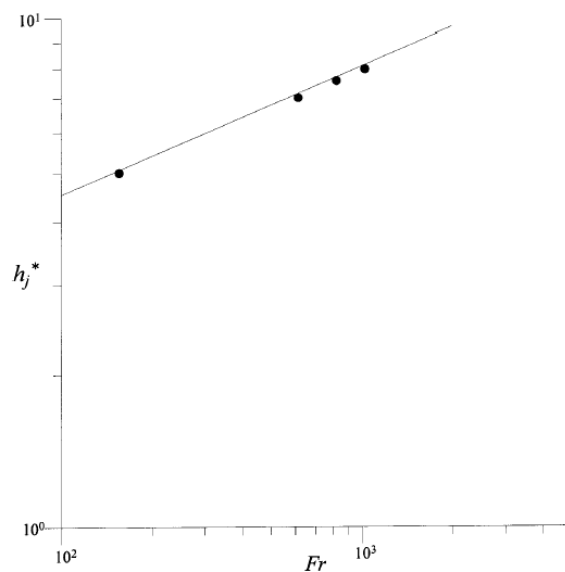


**Figure 1.20** Variation of jet height with Froude number (Fedorchenko and Wang 2004)

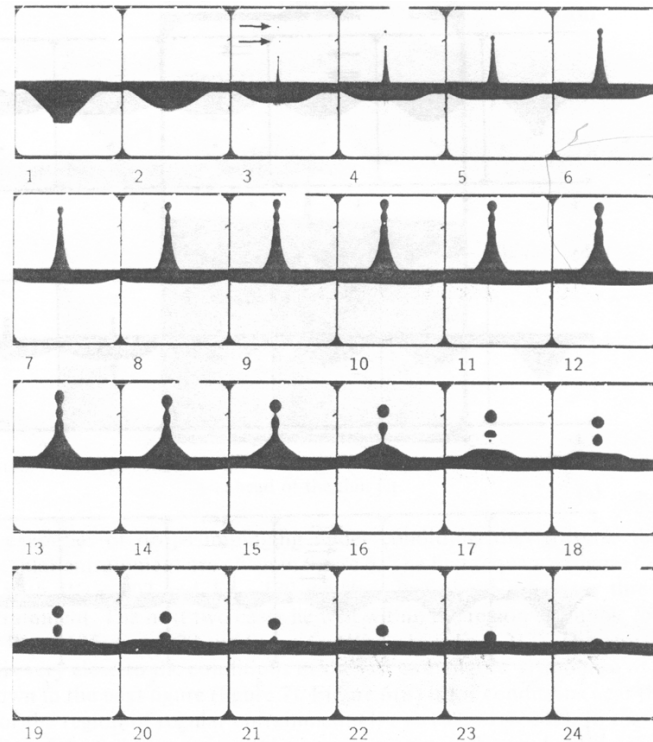


**Figure 1.21** Time sequence of thick jet formation (Rein 1996)

### **1.5.13 Secondary bubble entrapment**

Since the discovery of entrapped bubbles due to cavity collapse, many researches have sought to identify any other regions of bubble entrapment. Franz (1959) identified a region within the post-entrapment regime where bubbles do indeed form. Pumphrey and Crum (1989) give a rough diameter-velocity range in which the phenomena can occur. However, due to the variable nature (unpredictable and unrepeatably) of the phenomena, it has been labelled as “irregular” entrapment. In this thesis, it will be referred to as secondary bubble entrapment after Liow (2001). An example of how secondary bubble entrapment occurs is shown in Figure 1.22. As the cavity begins to collapse a stem structure is formed at the base of the cavity. This stem structure then breaks up leaving an entrapped bubble behind. The exact mechanism for the entrapment is still not entirely clear. However, Liow (2001) suggests that capillary instabilities may play a role in the entrapment mechanism due to the collapse of the air cavity being inherently unstable (Birkhoff 1956). One important point to note is that during secondary bubble entrapment a thick jet is produced rather than a thin jet as with primary bubble entrapment, since the effect of the stem break off is a localised phenomena. This is due to a change in the cavity dynamics which are still not fully understood in these region.

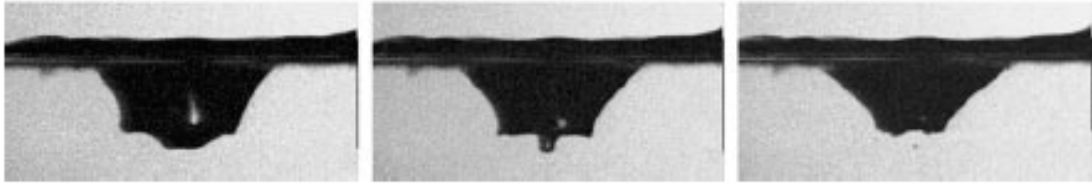


**Figure 1.22** Secondary bubble entrapment (Liow 2001)

#### **1.5.14 Surface bubbles**

When the impact velocity of the drop approaches terminal velocity, the crown thrown up by the impact can close to form a bubble floats on the surface (Franz 1959; Engel 1966). Since most rain drops travel at a terminal velocity, bubble formation on the surface of liquid pools is a common sight when it rains. This phenomenon occurs due to the film losing momentum and mass as it grows in height until such a point that surface tension forces begin to control the process, pulling the film together and closing above the pool. The result is a hemi-spherical bubble residing on the liquid surface (Figure 1.23). Very little work has been conducted in this area mainly due to the practical difficulties of imaging a drop that is falling from approximately 10 metres above the pool. The only other examples of work conducted in this area come from Mutchler and Hansen (1970) and Hallett and Christensen (1984). Neither of the aforementioned authors speculate on any lower limit for this process (*i.e.* what Froude number is required to entrap a surface bubble). From the limited photographic evidence shown by Hallett and Christensen (1984) that a downward jet associated with the film closure and the thick jet associated with cavity collapse do interact with the film. None of the aforementioned authors provide any discussion on the interaction of the upward jets with the thin film either. Furthermore, apart from the analytical work of Engel (1966) to predict the maximum cavity depth for such impacts, scant information is available regarding on how the height of the splash canopy scales as well as any velocity or time scales for the whole process. Therefore, there is scope for more research to be conducting in this area considering its immediate application to raindrop impacts.

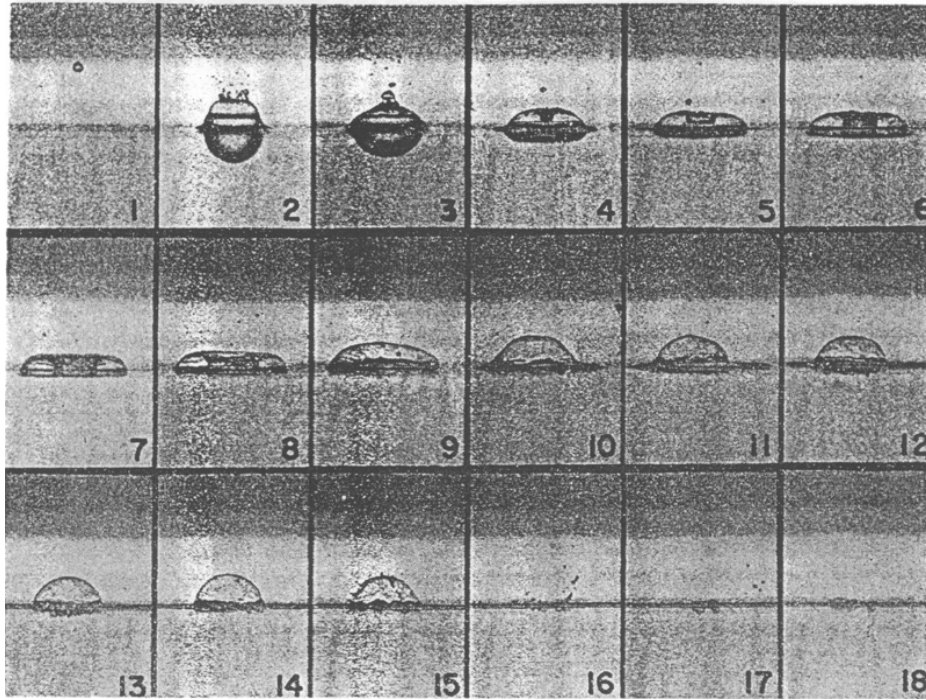


**Figure 1.23** Surface bubble on surface due to high velocity impact (Franz 1959)

## 1.6 Allied Splash Phenomena and Parameters

### 1.6.1 Influence of impact angle

When the drop impacts the surface at an oblique angle, (from the horizontal) the drop can either coalesce or bounce off the liquid surface. The phenomena of drops impacting at oblique angles had not been studied thoroughly until Jayaratne and Mason (1964) conducted an extensive investigation. Their results suggest that the transition between coalescence is not clearly defined rather it is more sinusoidal in nature. There are several angle ranges from the horizontal to the vertical where the drops coalesce, while in other angle ranges the drops bounce. Leneweit *et al.* (2005) have since conducted an extensive study into the influence of impact angle. In their study only a few cases of drop rebounding at angles less than  $14^\circ$ . In all other impacts the drops coalesced with the pool. This may be related to the size of the drops used. Leneweit *et al.* (2005) used drops in the order of 2 mm while Jayaratne and Mason (2005) used drops approximately  $500\ \mu\text{m}$  in size. Leneweit *et al.* (2005) primarily investigated the coalescence characteristics spreading patterns associated with oblique impacts. Using dyed drops and shadowgraph techniques Leneweit *et al.* (2005) show an extraordinary series of images highlighting the different spreading morphologies present (Figure 1.24). Leneweit *et al.* (2005) showed there are several different zones of drop spreading. The transition between the various regimes was highly discrete rather than continuous This suggests that must exist some critical thresholds for drop velocity and impact angle that once passed induce a marked change in spreading behaviour. Leneweit *et al.* (2005) additionally showed that a lamella (similar to the ejects sheet of Thoroddsen (2005)) can be formed at the front of the impacting drop under certain conditions. They found a critical  $We > 10$  suppresses lamella formation while a  $We < 10$  promotes lamella formation. The production of the lamella was also observe to increase the spreading velocity by a factor between 1.1 to 1.6 of the impact velocity, suggesting that the onset of lamellar should produce a change in spreading pattern. Leneweit *et al.* (2005) also observed that at impact angles less than  $22^\circ$  no immersion of the drop fluid was observed. At higher  $We$  numbers Leneweit *et al.* (2005) postulated that vorticity generated at the contact of the two surfaces advects some of the drop fluid into the pool, similar to what occurs in vortex ring formation.

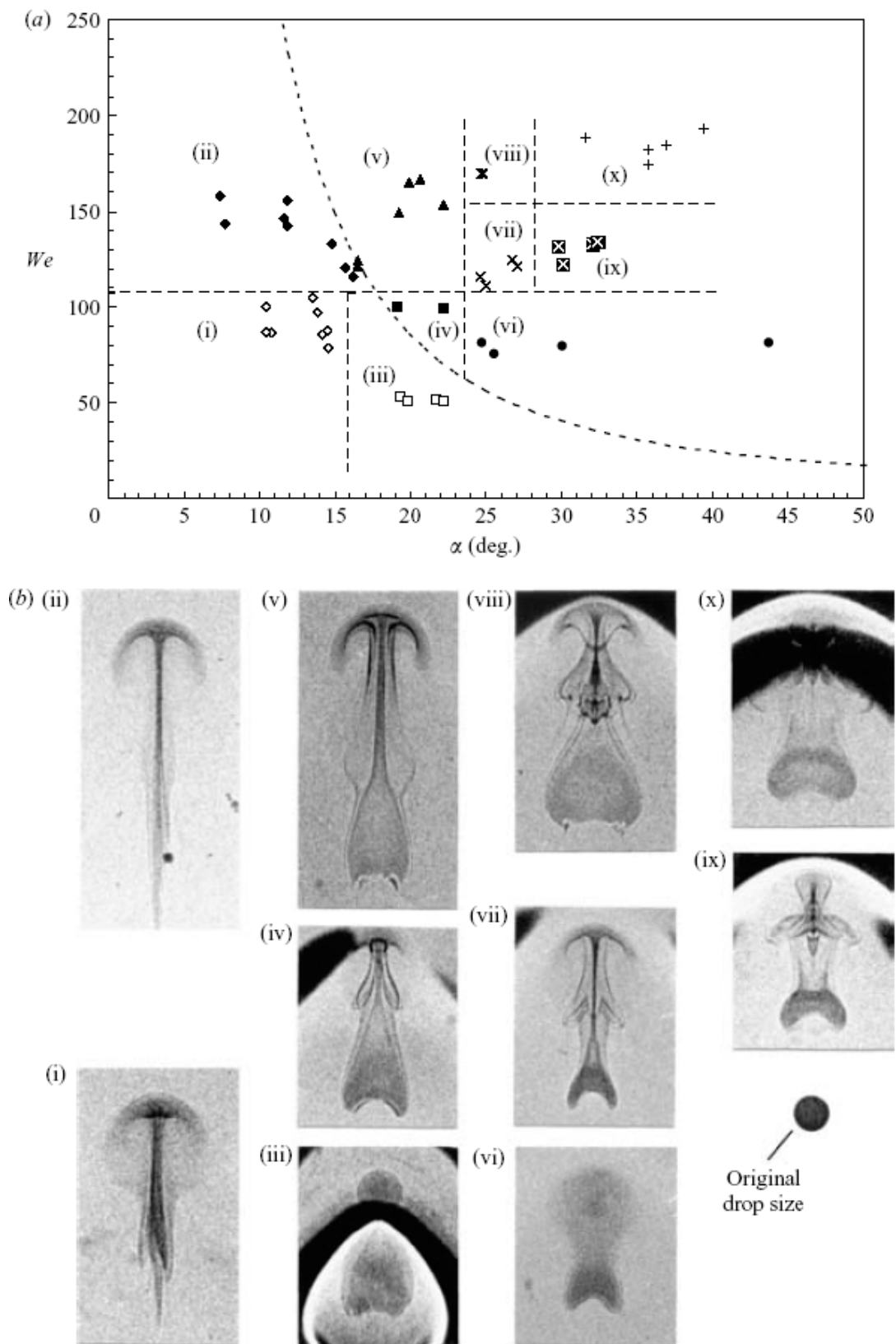


**Figure 1.24** Various spreading morphologies for oblique impacts (Leneweit *et al.* 2005)

### 1.6.2 Influence of pool depth

The phenomena resulting from the drops impacting on deep pools has already been extensively discussed. Thus this section surveys the work on the effects of shallow pools and thin films on the splashing process. A variety of experimental studies have been conducted on the effects of shallow pools (Hobbs and Osheroff 1967; Macklin and Hobbs 1969; Tuong and Painter 1974; Ferreira and Singer 1985). Hobbs and Osheroff (1967) showed some interesting effects induced by the shallow pool on the thick jet. They observed that at  $h_{pool} / d_d = 1$  the thick jet formed rose to around 0.5 cm. As they increased the film thickness to approximately  $h_{pool} / d_d = 3$ , the maximum height of the jet was observed to peak at approximately 2.5 cm. Increasing the pool depth even further, a drop off and flattening out of the maximum jet height to 1.8 cm was observed.

Drops impinging on thin liquid films is of significant interest in many industrial applications where the surface of a product is successively coated. The thin liquid layer generally ranges in size from a few millimetres to a few micrometers. Usually these situations arise when consecutive drops have impacted on a dry surface leading to the build up of thin liquid layer. The behaviour of drop impacts on thin films has been examined by (Levin and Hobbs 1971; Macklin and Mextaxas 1976; Wang and Chen 2000; Sivakumar and Tropea 2002; Rioboo *et al.* 2003) as well as many detailed numerical and theoretical studies (Yarin and Weiss 1995; Davidson 1998; Weiss and Yarin 1999). In thin film impact the most prominent structure observed is a thin filament thrown up from the impact site that resembles the crown formation (Figure 1.25).



**Figure 1.25** Crown formation in thin liquid film (Rioboo *et al.* 2003)

### 1.6.3 Influence of temperature

One of the only studies to examine the effect of temperature on liquid-liquid impacts was by Manzello and Yang (2003). In this study the impact pool was heated from underneath. Three different pool temperatures were evaluated 20°, 60° and 94°. Manzello and Yang (2003) observed that at higher pool temperatures the onset of jetting required a much lower Weber number than for the pool at ambient temperature. Manzello and Yang (2003) attributed this change to a change in the maximum cavity depth. They suggest at higher pool temperatures more of the initial impact energy is dissipated inhibiting cavity formation. However, it is more likely that a change in surface tension associated with the higher fluid temperatures changes the cavity formation dynamics.

### 1.6.4 Influence of drop size

Most of the theoretical and numerical work conducted in liquid-liquid impacts has assumed a spherical drop shape. However, in reality when the drop strikes the liquid surface, it can take on one of three forms at the instant of impact: oblate, prolate and spherical. As already discussed in section 1.5.7, the drop phase can have a significant bearing on the shape of cavity formation and thus all subsequent phenomena.

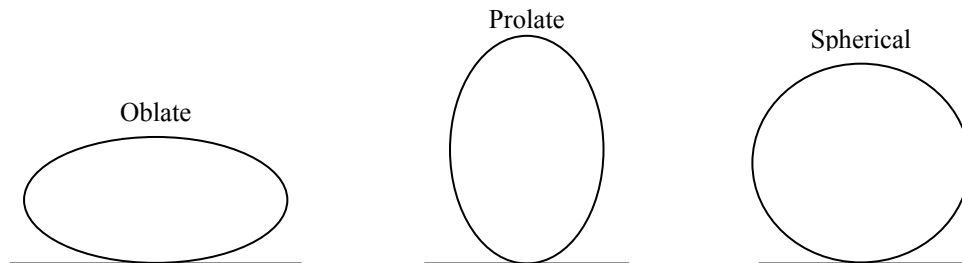


**Figure 1.26** Three forms of possible impact

These different drop shapes are caused by oscillations of the drop as it pinches off from its source. As the drop pinches off, a disturbance is created on the drops surface, distorting the drops shape. Surface tension attempts to restore the shape of the drop, however, gravitational forces tend to oppose this restoring force. Thus, these competing forces then turn the drop into a vibrating liquid mass. Theses oscillations become more exaggerated as the size of the drop increases and it takes a longer to damp out. Thus, as the drop size increases and release height is lowered, it is more probable that the drop will impact with a non-spherical shape affecting the dynamics of cavity formation.

Work performed by Cai (1989) has attempted to quantify the effect of drop eccentricity. His results suggest that a drop larger than 4 mm in diameter will have an eccentricity of approximately 0.1. Here the eccentricity is defined as the major axis length minus the minor axis length all divided by the major axis length. To mitigate any oscillatory effects the eccentricity of the drop needs to be kept below 0.02.

### **1.6.5 Surface Tension and Viscous Effects**

Many of the flow phenomena in liquid-liquid impacts have been described as being controlled by surface tension, viscous and inertial forces. Davis Philip (1960) conducted experiments to see the effects of glycerol on drop impact. Before this study all drop impacts had been conducted using water or milk. Two quantities were measured in this study. One quantity was the time taken for the crown to form and second was the time taken for the cavity to fully form. Based on the results recorded, Davis Philip (1960) attempted to apply an empirical correlation to his observations. He derived a formula using scaling analysis that suggested the timescales for these events to occur was a function of Reynolds and Froude numbers. However, errors in the order of 20% were observed. Therefore, the trustworthiness of this data is questionable. Prosperetti and Oguz (1993) describes the bounds of primary bubble entrapment for fluids of varying viscosities (Figure 1.27). This plots highlights that when the viscosity of the fluid is changed, the region of primary bubble entrapment differs from that of water. This implies that the cavity formation and collapse process is sensitive to changes in viscosity not just surface tension and inertia. Just how sensitive the bubble entrapment process is to changes in viscosity is still not clear, nor is it clear for any other phenomena. Thus, there is scope for a more thorough investigation to be conducted in this area.

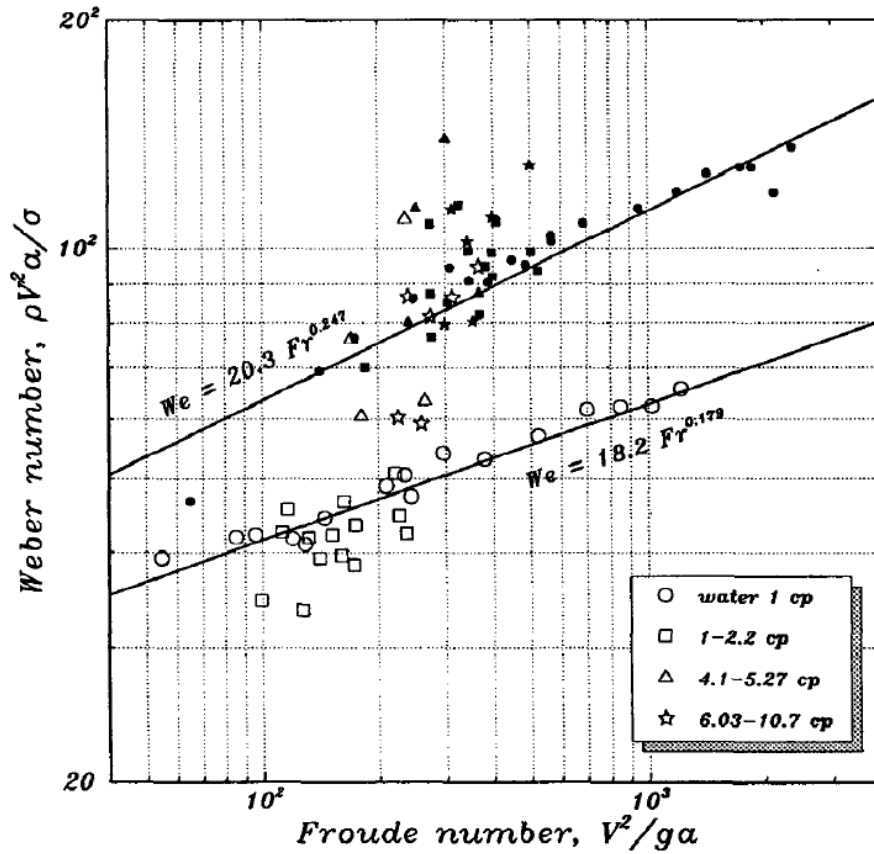
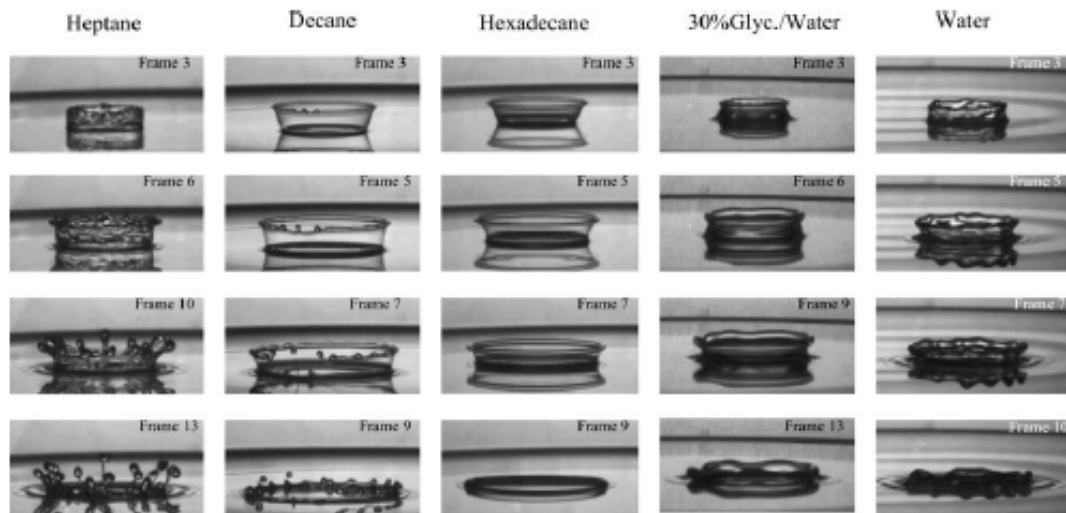


Figure 1.27 Bubble entrapment for varying viscosity fluids (Prosperetti and Oguz 1993)

Wang and Chen (2000) did experiments on different viscosity fluids. They reported that higher viscosity fluids inhibit splashing at lower Weber numbers. This would tend to indicate that viscous forces play a role in the break-up of the film thrown up by the impact. A recent study by Vander-Wal *et al.* (2006) has sought to investigate many of these effects by using a wide range of fluids with different viscosities, densities and surface tensions (Figure 1.28).



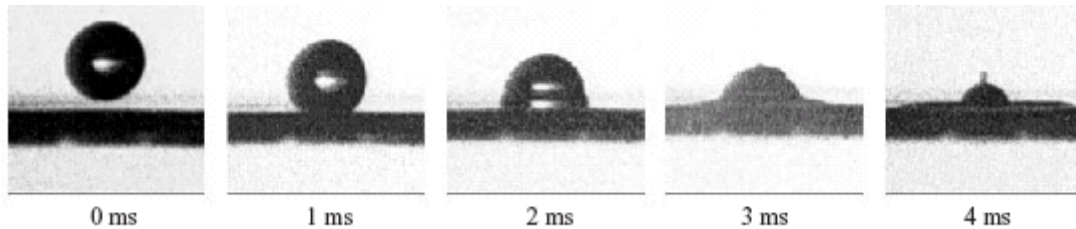
**Figure 1.28** A 2.7 mm drop impacting at 2.17 m/s on a thin film (Vander-Wal *et al.* 2006)

Figure 1.28 highlights several different crown formations from a variety of different fluids. Heptane and decane appear to readily break-up while the hexadecane, glycerol mix and the water impacts do not. Examining the surface tension of each of the fluid it can be seen that heptane, decane and hexadecane have a surface tension approximately one-third that of water. Therefore, it appears lowering the surface tension promotes film break-up. However, if surface tension was the only controlling factor then the hexadecane case should also break-up. If we now examine the viscosities of each fluid we see that hexadecane has a viscosity almost three times that of water, heptane and decane. Thus, it appears viscosity also plays a key role in the splashing process not just surface tension. Examining Figure 1.28 it appears viscosity's main role is to damp out any disturbances. The two highly viscous cases (hexadecane and glycerol mix) exhibit minimal capillary waves on their surfaces. In summary, the effects of viscosity and density are intertwined within many of the flow phenomena within liquid-liquid impacts. Changing each or both of these properties can have marked effects on the flow behaviour observed.

### 1.6.6 Apex drop

At low impact velocities, the speed of the propagating capillary waves is faster than the rate at which the drop actually collapses. The result is the capillary wave coming together at the top of the drop before the drop squeezing off a small droplet before the drop itself has been enveloped by the bulk fluid. A comment in regards to apex drops formation was made by Peck and Sigurdson (1994). They suggested the impact of the

apex drop on the cavity may be inducing a small vortex ring to be shed from the cavity. More recently, apex drops were revisited by Liow (2001) and briefly discussed. For the case shown in Figure 1.29 the drop impacting the surface is secondary drop produced by the initial splash. However, an exhaustive study of this phenomena is still absent to date.



**Figure 1.29** Apex drop formation from a secondary drop  $Fr = 9.5$ ,  $We = 6.9$  (Liow 2001)

### 1.6.7 Bubble acoustics

It has always been known that liquid-liquid impacts can emit audible sound. Much of the work associated with detecting noise in liquid-liquid impacts has been concentrated on the effect rain and snow has on lakes and oceans (Scrimger 1985; Scrimger *et al.* 1987). In all of this work a strong peak at 14 kHz was observed. The exact reason this signal was not understood until Pumphrey and Crum (1989) carried out a studying using synchronised hydrophone and video data (Figure 1.30). In Figure 1.30 the initial impact of the drop emits a minimal acoustic signal. While the entrapment of the gas bubble due to cavity collapse (frame h) of the cavity shows a marked acoustic response. Pumphrey and Elmore (1990) also explored high velocity impacts in the post entrapment regime with little acoustic response.

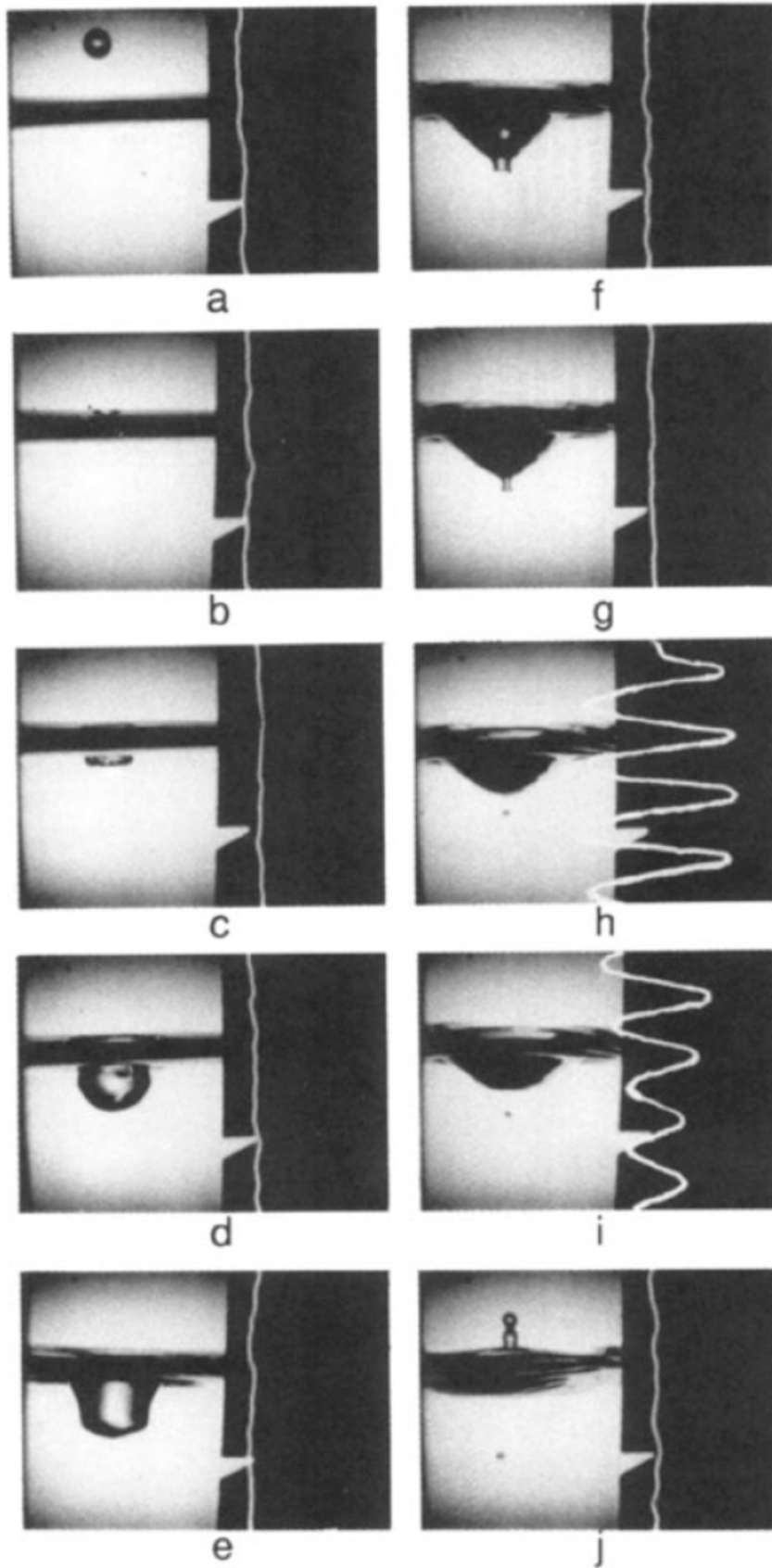


**Figure 1.30** Video and acoustic traces of the primary bubble entrapment process (Pumphrey and Crum 1989)

### 1.6.8 Entrapped Bubbles Bursting at the Free Surface

Bubbles entrapped during liquid-liquid can come to the surface and burst to produce jets that rapidly break-up. This phenomena is thought to be the mechanism by which salt is transferred from the ocean to the air Blanchard and Woodcock (1957). Therefore, the main researchers investigating this area are primarily navy and marine scientists. Thus, the main media these studies have been carried out, is seawater (Blanchard and Woodcock 1957; Blanchard and Syzdek 1981, 1988; Blanchard 1989, 1990; Spiel 1994, 1995, 1997). Notwithstanding this, Spiel (1995) carried out a detailed investigation of the drop velocity and size distribution from bubbles bursting in freshwater (Figure 1.31). Here the exit velocity of the first drop is proportional to the bubble size. The actual drop velocities and diameters are very similar to velocities and sizes reported by Liow (2001) for the thin high-speed jet. Therefore, it is quite possible the same mechanism inducing break-up of the liquid jets from bubbles bursting is also responsible for the break-up of the thin high-speed jet. However, the two phenomena are not exactly the same. In Figure 1.31 the majority of cases only four to five drops are produced. In the break-up of the thin high-speed jet, more than eight secondary drops have been observed. While much work has been conducted on analysing the jet break-up the exact physics governing the collapse of the bubble formation of these jets is still not well understood.

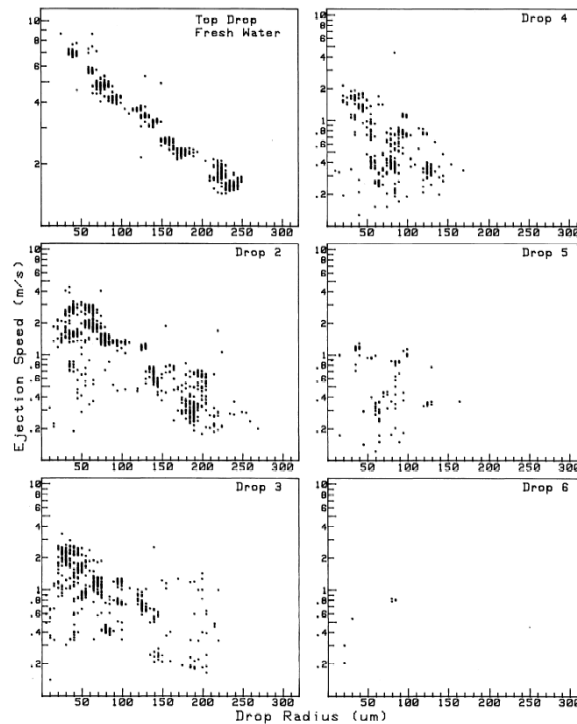


Figure 1.31 Drop size and velocity distribution from bursting bubbles (Spiel 1995)

## 1.7 Particle Image Velocimetry (PIV)

In the past three decades, several experimental techniques have been described to capture instantaneous velocity fields in fluid flows. The PIV technique grew out of the work by Meynart (1983) on Laser Speckle Velocimetry. Details on the development and history of the technique are contained in several review papers (Adrian 1991; Prasad 2000). PIV is just one of many techniques in the general area of pulsed light velocimetry. In PIV, particles with similar density to the fluid are used as tracers. The particles are illuminated by a light source (laser) and the subsequent displacements of the particles are recorded on images. The images are then divided into equally sized interrogation areas and correlated to provide a velocity map of the flow. The velocity map contains direction and magnitude of the velocity at each interrogation area.

Most PIV systems used hitherto have framing rates of 30Hz or less. For a fast transient event such as the evolution of a vortex ring, previous researchers (Morton *et al.* 2000) have built up a picture of the vortex ring evolution by matching frames from separate experimental runs. For an impacting water drop, the flow field resulting from the impact is extremely sensitive to the impact conditions and small variations from drop to drop result in substantial variations in the flow field after about ten milliseconds. An accurate interpretation of the developing flow field from drop impact requires capturing the flow event of a single impacting drop, rather than a reconstruction from multiple drops. Notwithstanding this Morton *et al.* (2000) were able to experimentally measure the radial and axial velocities of the vortex rings and show a reasonable correlation to numerical results. Recently, the use high framing rate PIV (HFR-PIV) systems for measuring transient events have been reported (Shinohara *et al.* 2004; Towers and Towers 2004) but no applications of HFR-PIV have been described for liquid-liquid impacts.

Machu *et al.* (2001) performed an extensive series of PIV experiments using standard PIV equipment to examine vortex ring formation and break up during a drop impact. In this study of sedimenting drops, the high density of particles used in the drop induced significant light scattering, resulting in the most critical flow data close to the drop boundary being compromised. Thus critical behaviours in this area may have escaped detection. More recently work performed by Mohamed-Kassim and Longmire (2003)

delve deeper into the PIV analysis of drop impacting. The framing resolution of the cameras was quite small at 572 x 432 pixels, while the framing rate was restricted to 500 fps. Several problems exist with the results presented in this paper. The particles used were 2  $\mu\text{m}$  in diameter and from the imagery presented, it appears the particles were clumping together making the results dubious at best. This meant the particles covered the interface trying to be observed, causing significant error. Furthermore, the density of the particles was almost three times the density of the liquid used in the experiment.

It is quite clear the PIV has significant potential to reveal the flow field around a splashing drop and provide a better explanation of the fluid mechanics in splashing process. However, poor experimental technique and consideration, coupled with restricted technology makes the published results to date questionable.

## **1.8 Summary**

The study of the liquid-liquid impact problem is of concern in many industrial and natural processes. Experimental observations dating back over 100 years have described a complex mix of phenomena. It has only been in the last decade that technology has been able to actually capture the finer detail of liquid-liquid splash. High-speed digital video cameras and PIV techniques will be used in this study to capture events in the microsecond range. The details of these experimental apparatus will be covered in Chapter 2.

Many researches have sought to carry out studies on individual phenomena in liquid-liquid impacts. This is useful for understanding individual flow features. However, the reader is left unaware of where the specific phenomena resides in the over all liquid-liquid impact spectrum. More importantly, the reader is not aware of how the phenomena being investigated may influence or be influenced by other events. Essentially a “big picture” view of the phenomena arising from liquid-liquid impacts has been lacking. Thus, the first objective of this study to use high speed video across a broad range of impact velocities and drop sizes to collect and categorise existing and new flow phenomena. In Chapter 3, this information will be used to compile a

comprehensive picture of the splashing morphology from liquid-liquid impacts to identify new phenomena and place existing flow behaviour in a broader context.

In terms of specific phenomena, there still exist many gaps in our current knowledge. In the area of cavity formation and collapse, the exact mechanisms and forces that govern cavity shape and size are largely unknown. At high impact velocities, the cavity expands with a hemi-spherical shape while at lower impact velocities the rates of expansion downward and parallel to the surface differ. This results in cylindrical and conical type cavities. The other aspect of cavity development is the collapse phase of the cavity. The exact mechanisms that induces cavity collapse and change the shape of the cavity as it collapses is still not clear. Therefore, the second objective of this study is to understand the physics of the cavity formation and collapse by using experimental techniques. This will be covered in Chapter 4.

Another important phenomena in liquid-liquid impacts that has not been investigated thoroughly is the mechanisms that give rise to the different types of jetting. In some cases the cavity collapses without any jetting (composed regime) while in other regimes the collapse of the cavity gives rise to both thin high speed jets (primary bubble entrapment) and slow moving thick jets (post-entrapment jetting). Furthermore, detailed descriptions of the size and velocity distributions of the secondary drops for the various modes of jetting have not been presented to date. Thus, the third objective in this thesis is to experimentally investigate the mechanisms that lead to the formation of jets in each regime and characterise the jets. These topics will be discussed in Chapter 5.

The other major aspect of liquid-liquid impacts and the one of most interest to the author is the formation of bubbles during the liquid-liquid impact process. Many modes of bubble entrapment have been identified during this review. The reasoning for the formation of bubbles in certain cases is well documented (Thoroddsen bubbles, primary bubble entrapment) but in other cases it is still unclear (Oguz bubble rings, thin film rupture in the composed regime). Thus, the final objective in this study is to understand the physics behind each mode of bubble entrapment. In addition where each bubble entrapment phenomena resides in the broad spectrum of impacting conditions will be delineated so certain bubble entrapment modes can be either promoted or avoided.

Finally, for practical purposes the volume of air each mode entraps will be quantified. These topics will be covered in Chapter 6.

In summary, the remainder of this thesis will be broken into the following chapters.

Chapter 2 – Detailed discussion on the experimental apparatus, experimental technique, analysis techniques and the experiments to be conducted to achieve the above objectives

Chapter 3 – Compilation of high-speed images and descriptions covering all flow behaviour observed in this study. Formation of detailed quantitative and qualitative maps of the splashing morphology.

Chapter 4 – Experimental investigation into the mechanisms that influence how the cavity forms and collapses by using PIV and high speed video.

Chapter 5 – Understanding how jets are formed and influenced by the collapsing cavity as well as characterising the secondary drops formed in each jetting regime

Chapter 6 – Examine all modes of bubble entrapment and quantify the amount of air each can entrap.

## CHAPTER 2 - EXPERIMENTATION

### 2.1 Introduction

The two main experimental techniques employed to study liquid-liquid impacts in this thesis are high-speed video and high-speed PIV. This chapter will describe the individual components used in each of these techniques. The different experimental configuration will also be described along with the analysis techniques employed. The specifics of each experimental run are described in 2.5.

### 2.2 Experimental Apparatus

#### 2.2.1 Drop generation and height control

An integral part of performing a study on the impact behaviour of small drops relies on the drops to be of a consistent size and shape. In this series of experiments three different sized flat tipped needles (Hamilton 33G, 26G and 20G) were used to form drops with diameters of  $2.06 \pm 0.060$  mm,  $2.53 \pm 0.044$  mm and  $3.13 \pm 0.044$  mm respectively. The rationale behind using flat tipped needles is that they produce drops with a more consistent diameter. The needles themselves were held in the dropper arm shown in Figure 2.1 that is oriented perpendicular to the liquid surface. The drop liquid was pumped into the needles via a Cole-Palmer 74900 Series syringe pump operating at a constant flow rate. Operating with a constant flow rates will minimise diameter variations from drop to drop. The time between drops was kept to a minimum of 5 seconds in order to reduce the influence of the preceding drop on the dynamics of the flow. The tip of the needle was positioned above the laser beam projected by a Laserex LDP-350AV laser pointer. Directly opposed to the laser beam was a Centronics BPX65 photodiode with a 5 ns response time to detect the falling drop. When the falling drop broke the laser light beam, a 5V TTL signal was sent to the Redlake cameras to initiate recording. The dropper arm was mounted on a computer controlled 3D traversing system with a spatial resolution of  $\pm 12.5$   $\mu$ m. The traversing system was capable of extending the dropping arm 1.3 m above the impact tank. This equates to an approximate impact velocity of 4 m/s with a Froude number of 815. However, experimental observations were hard to achieve at heights above 1 m due to localised

air velocities deflecting the drop from its vertical drop path and causing the drop to miss the target area.

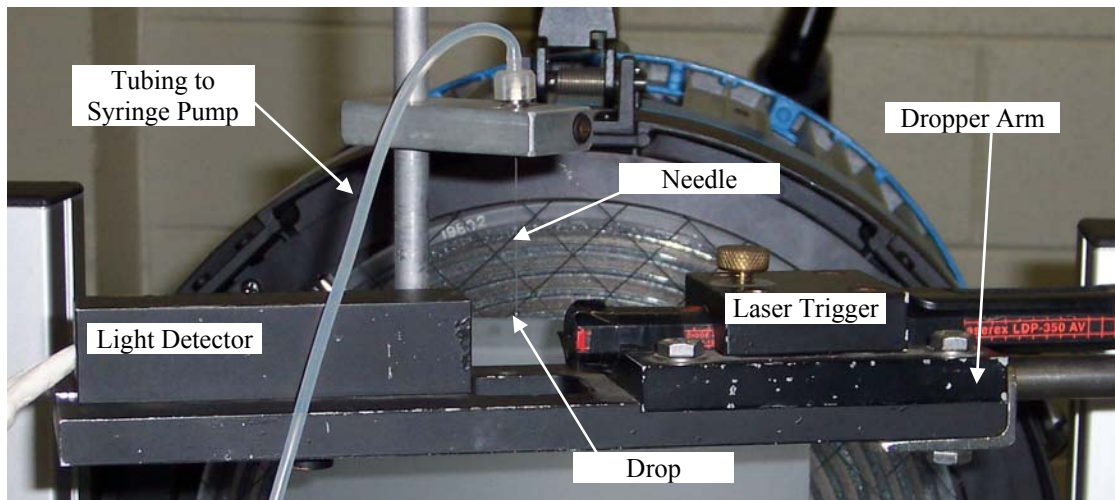


**Figure 2.1** Liquid dropping arm

### 2.2.2 Impact Pool

The impact pool was made of transparent glass sheets 3 mm thick with overall inner dimensions of 200×200×100 mm. This pool was placed inside a larger overflow tank measuring 300×300×50 mm (Figure 2.2). The water level in the impact pool was brought level with the top edge of the impact container. This makes the depth of the pool approximately 50 times greater than the drop diameter thereby eliminating any effects associated with the bottom of the pool. Prior to any experimentation occurring, the top layer of water in the impact pool was removed for two reasons. Firstly, the free surface that is in contact with the rim of the tank tends to create a meniscus, from the adhesive surface tension forces, that obscures the splashing event. Secondly, foreign bodies such as large dust particles can build up on the liquid surface and change the surface tension of pool liquid to such a degree that the repeatability of the experiments can be compromised. Therefore, every hour during experimentation, the pool surface was skimmed to minimise this problem. One of the many assumptions made in the experimental design is that the liquid surface is free from any disturbances (*i.e.* surface waves) when the drop impacts. This can be quite simply achieved by having sufficient time between impacts so that the surface waves are damped out before the next drop impacts. A time period of at a minimum of 5 seconds was allowed between impacts to ensure no surface disturbances affected the splashing process.

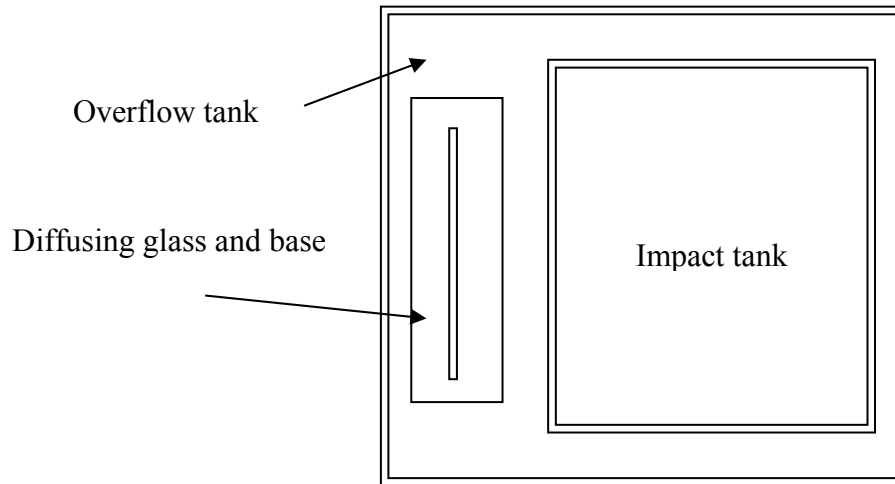


**Figure 2.2** Sketch of impact tank and overflow tank

### 2.2.3 Liquids

Steam distilled water from the same source was used for both the pool fluid and impacting drop fluid. Every hour a portion of the pool fluid was exchanged with new fluid to ensure consistency and repeatability during the experiments (Hsiao *et al.* 1988). A thermometer resided in the liquid bath to monitor the temperature at all times during experimentation. Viscosity and surface tension properties were extracted from based on the temperatures recorded during experimentation (Table 2.1). A glass thermometer, placed in the bath, monitored the temperature. In certain cases, it was desirable to dye the impacting fluid with a 0.02M  $\text{KMnO}_4$  solution to help visualise the flow.

**Table 2.1** Viscosity and surface tension for different temperatures (Munson *et al.* 1998)

Temperature (°C)	Density ( $\text{kg/m}^3$ )	Viscosity ( $\text{Ns/m}^2$ )	Surface Tension (N/m)
20.0	998.2	$1.002 \times 10^{-3}$	0.0728
21.0	997.95	0.982	0.0726
22.0	997.7	0.961	0.0725
23.0	997.5	0.941	0.0723
24.0	997.2	0.920	0.0722
25.0	997.0	0.900	0.072

#### 2.2.4 Digital Cameras

A pair of Redlake HG-100K cameras was used for image recording, the technical specifications are described in Table 2.2. The HG-100K has a maximum resolution of 1504 x 1128 pixels at 1000 frame per second (FPS). The HG-100K can increase its framing rate by reducing its resolution. Some common framing rates and associated resolution are shown in Table 2.3. To facilitate data and power transfer, the Redlake cameras were connected to the Redlake Hub Sync Unit. For power, the hub was connected to a Sorensen DCS40-25E variable voltage and current power supply. Data was transferred to and from the computer by utilising an Allied Telesyn AT-2970TX gigabit Ethernet card in a Dell Precision 450 workstation. The resolution, framing rates, exposure timings, depth of field, optical magnification used during experimentation varied depending on camera position, phenomena being studied and whether the cameras were being used for high-speed photography or PIV. The specific values used in each case are described in the following sections 2.3.1 and 2.3.2. In all cases during experimentation, a Nikon Micro 105mm lens was attached to the cameras. According to manufacturers specifications the maximum synchronisation error between the two cameras is  $\pm 2.5 \mu\text{s}$  and 6 ns per metre of cable. The maximum error expected will be within  $\pm 2.6 \mu\text{s}$ . For a framing rate of 30,000 FPS the time between frames is 33.3  $\mu\text{s}$ . This equates to approximately a maximum of 8% timing error between the two cameras.

**Table 2.2** Technical specifications of the Redlake HG-100K cameras

Camera Characteristic	Specification
Sensor type	CMOS
Max. resolution	1504x1128
Memory capacity	2GB
Min. exposure time	5 $\mu\text{s}$
Colour	Monochrome
Bit depth	8 bit
Impact resistance	100G @ 5ms
Sensitivity	ASA400
Pixel edge length	12 $\mu\text{m}$

**Table 2.3** Maximum resolution possible for a given FPS rate

<b>Frames per Second</b>	<b>Max. Resolution (pixels)</b>
30, 60, 120, 250, 500, 1 000	1504×1128
2 000	1024×768
3 000	832×624
5 000	640×480
10 000	416×312
20 000	256×192
30 000	192×136
50 000	128×100
100 000	96×96

### 2.2.5 PIV Laser

The unique challenge in attempting to experimentally capture instantaneous velocity fields at high framing rates (1000+ FPS) relies on high repetition lasers with a stable output between pulses. In this project, a Lee Laser LDP-100MQG Nd:YAG laser was utilised. The technical specifications of the laser are shown in **Error! Reference source not found.** The laser itself was mounted on an optical breadboard, which was in turn mounted on a pneumatically controlled vibration isolation bench. The output of the laser was redirected through an articulated light arm (Figure 2.3). Attached to the end of the light arm was the light sheet optics. The laser light sheet optics consisted of a Dantec 80x73 base module with a Dantec 80x75 wide-angle adaptor to increase the spread of the light sheet. A Dantec 80x71 focusing lens controlled the thickness of the sheet.

An important component of the laser and has a direct impact in performance characteristics of the laser, is the q-switch. The use of q-switching enables two laser light pulses to be released in quick succession so extremely fast pulse rates can be achieved. For longer time delays between pulse pairs, the time for energy build up becomes longer, resulting in overall higher power output. Thus, an important characteristic of the laser is the relationship between energy output and the time delay between pulses. Using a Gentec SOLO PE power meter the output power of the laser was measured for a variety of different pulse delays across different supply amperages (Figure 2.4).

**Table 2.4** Technical specifications of the PIV laser

<b>Laser Characteristic</b>	<b>Specification</b>
Wavelength	532 nm
Beam Diameter	2.5 mm
Divergence	4 mrad
Pulse Duration	75-250 ns (depending on frequency)
Time Between Pulses	20-1000 $\mu$ s
Pulse Pair Frequency	0.3-10 kHz
Polarization	Linear
Pulse Energy: Each pulse	0.7-12 mJ
Peak Pulse Power: Each pulse	1.4-160 kW
Pulse Energy Stability	< 3% RMS

Figure 2.4 shows the relationship between output power and pulse delay is highly nonlinear past 200  $\mu$ s where a rapid drop off in output power with increasing delay occurs. That is, increasing the delay time between pulse pairs only provides a minimal performance increase. A significant performance increase can be achieved by increasing the supply amperage. For the low supply amperage of 9 amps, the performance is dismal. Increasing the amperage to 11 amps an almost ten fold increase in performance can be seen. Further increasing the power supplied to 13 amps gives a three fold increase in output power. Thus, in general if a higher output power is required it is best practice to increase the supply amperage rather than increasing the delay time. However, there are limits on maximum supply amperage. According to manufacturer's specification, the laser is restricted to only 15 amps before damage to the diode can occur.

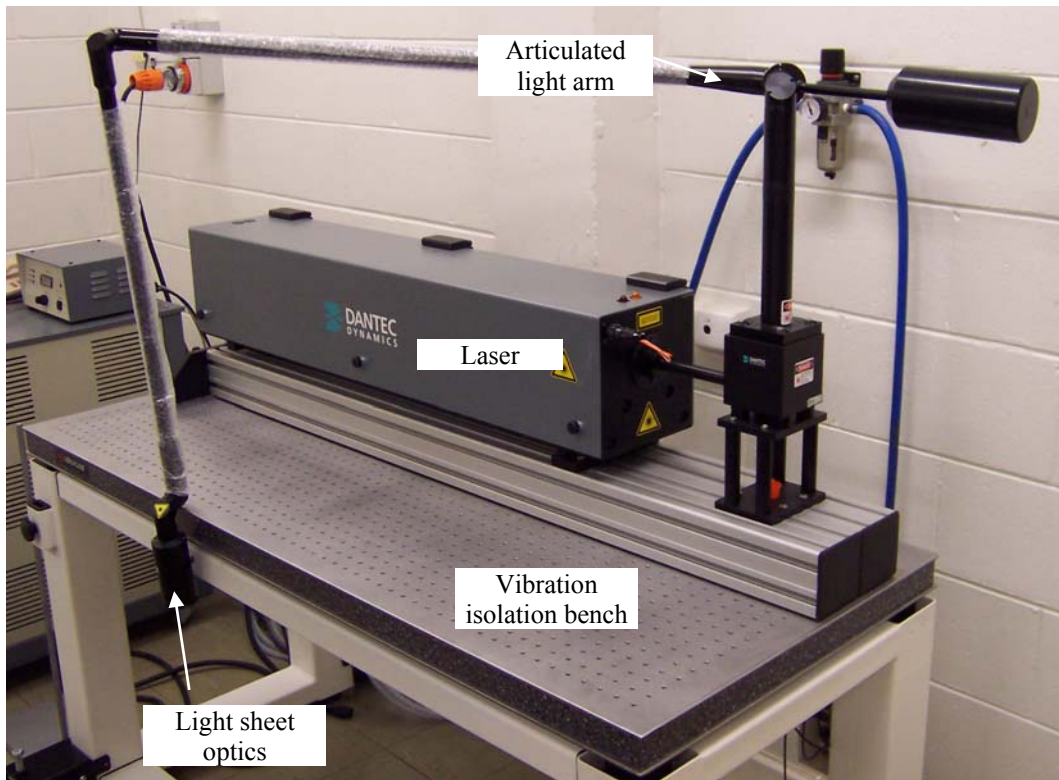


**Figure 2.3** PIV laser on mount with light arm

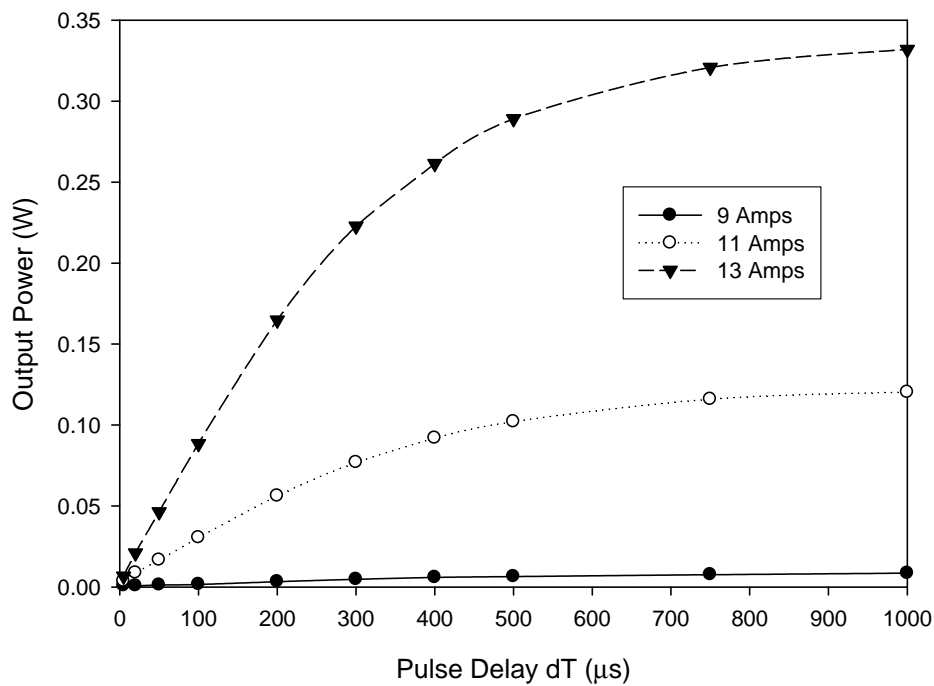


**Figure 2.4** Output power of the Nd:YAG laser for various pulse delays at different supply amperages

## 2.3 High-Speed Video Configuration

### 2.3.1 Backlighting

The most common technique of imaging the splashing process is the use of backlighting. Backlighting relies on placing the light source directly behind the impact pool so that the area of interest lies between the camera and light source. This enables the profile of the cavity, which forms on impact, to become visible by virtue of the light it obstructs. While this method allows for the edges around the periphery to be crisp and sharp, generally information on what is occurring within the darkened area is lost. The experimental setup for backlighting techniques is shown schematically in Figure 2.5. The Redlake HG-100K cameras are used here to provide synchronised details above and below the water bath. Depending on which features were being photographed, the resolution and framing rate were refined to capture the most amount of detail at the highest framing rates possible. The camera that was positioned to capture the details below the surface had an exposure time of  $5\ \mu\text{s}$  with a 1:1 magnification. A  $5\ \mu\text{s}$  exposure time is required to freeze the splash. With any exposure time higher than this value, the rapid motion of the impact becomes blurred and unsuitable for analysis. The second camera positioned above the surface was generally only used to capture the drop prior to impact and any jetting that may occur.

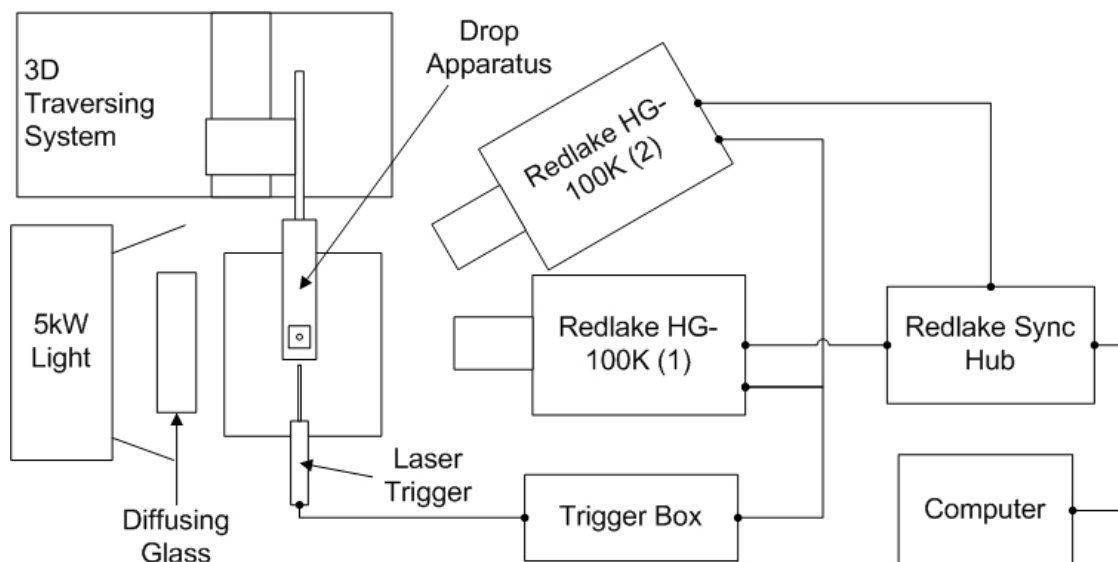
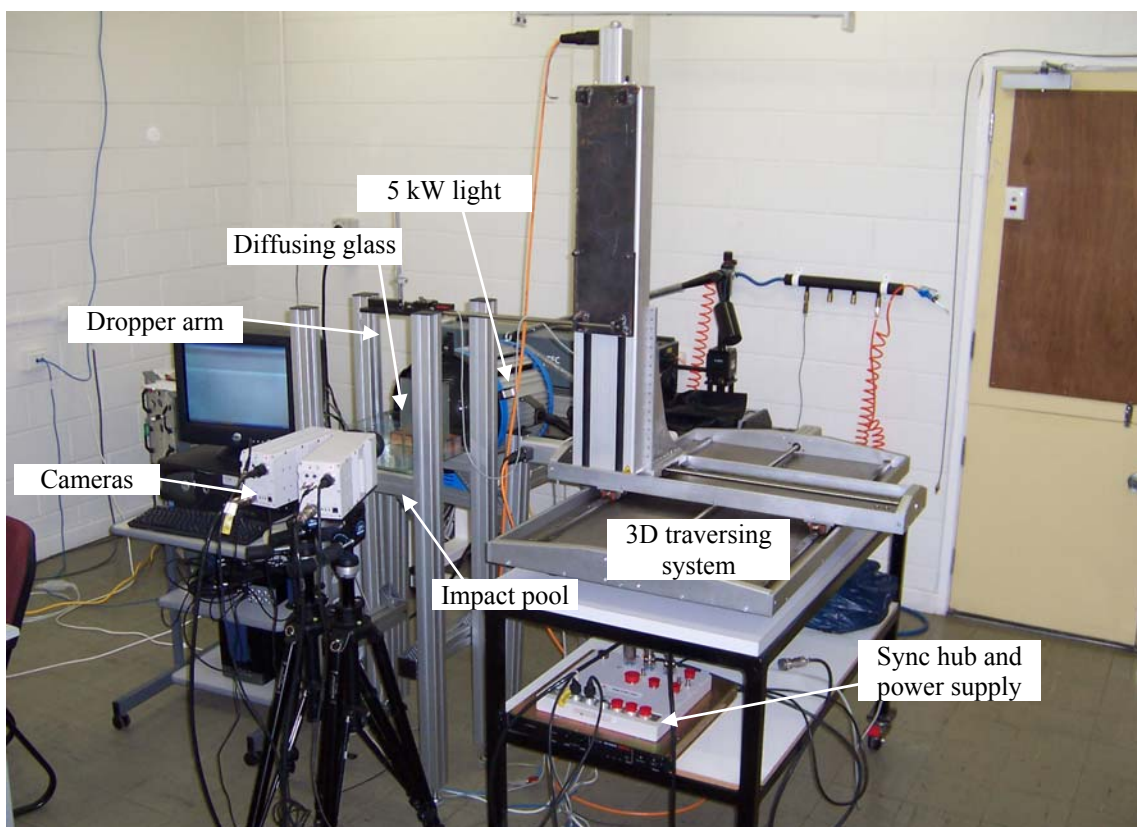


Figure 2.5 Schematic drawing of experimental apparatus

The f-number was set to 11 on both lenses as this f-number was found to provide the best trade off between depth of field and available lighting. For sufficient back lighting at a 5  $\mu$ s exposure timing an Arri Studio 5 kW tungsten-Fresnel lamp was used to saturate the area with light. The Fresnel lens contained in the lamp produces a subtle light and dark banding that can cause problems when analysing the images. To combat this problem a 180 $\times$ 180 mm diffusing glass pane was placed between the lamp and the target being filmed to provide an even distribution of light. The 5 kW light was only turned on for a brief period (3 secs) when recording was taking place to reduce the thermo-capillary waves that can cause disturbances on the liquid surface. Camera timing, exposure, frame rate, recording and processing were managed and controlled by Redlake's Motion Central software. The final experimental setup is shown in Figure 2.6.



**Figure 2.6** Experimental setup for high speed video

### 2.3.2 Photography down the cavity

In some cases, it was desirable to actually look into the forming cavity to extract information about the splash. The unique problem when looking into the cavity is that the incident light is reflected in all directions by the free surface and curved cavity. Additionally, with the camera being inclined on an angle the depth of field must be increased to keep the entire cavity in focus. To compensate for the increased depth of field requirement the f-number was increased to f22. A smaller aperture results in a vastly reduced light intensity reaching the camera. When this effect is combined with the severe light scattering induced by the free surface and cavity the 5 kW light alone is not powerful enough. Therefore in order to intensify the incident light an Edmunds 18.5" Fresnel with an focal length of 24" was used in conjunction with a piece of Borafloat IR glass to protect the Fresnel from the extreme temperatures generated by the light was mounted on the 5kw light. The protective glass was covered with a diffusing paper to evenly light the cavity.

The most difficult challenge in performing down cavity imaging is obtaining even lighting across the cavity as it forms and collapses. Many of the methods attempted revolved around attempting to contain as much of the light as possible within the target area. To this end aluminium sheet and stainless steel were used to reflect any light back into the impact zone. However, their surfaces promoted an intolerable amounts of light scattering for the exposure times being used here. It was found the only way to effectively return some of the light back into the camera was with small mirrors (100 mm × 100 mm). The camera was inclined at 60 degrees to the horizontal and roughly 30 degrees from the vertical. The 5kW light was placed at an equal angle to this. A mirror was placed at the bottom of the pool and inclined to reflect the light behind the impact site. The angle of the light also allowed for the illumination the cavity from the top as well as the reflected light from the mirror to even up the lighting. While the above measures improved, the illumination of the cavity there was still not sufficient light available to persist with a 5  $\mu$ s exposure time. The best trade off between image blurring and light intensity was made with a 20  $\mu$ s exposure time. The final arrangement for the down cavity configuration is schematically shown in Figure 2.7 and actual apparatus in Figure 2.8.

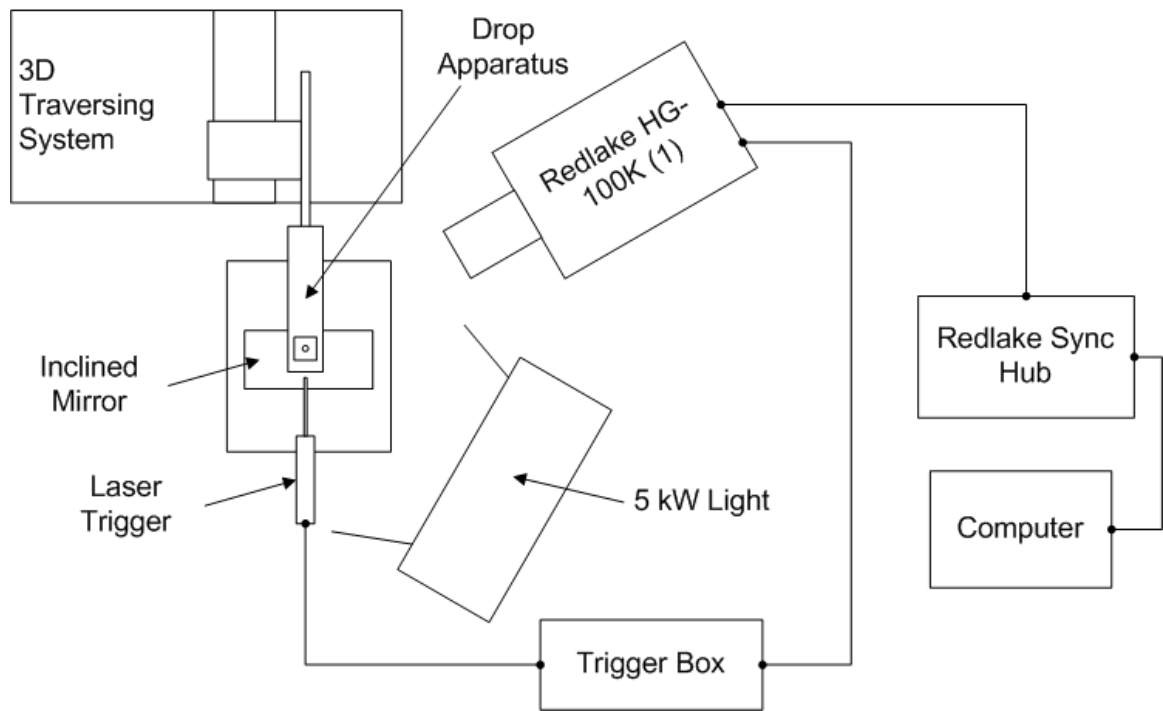


**Figure 2.7** Schematic of down cavity lighting configuration

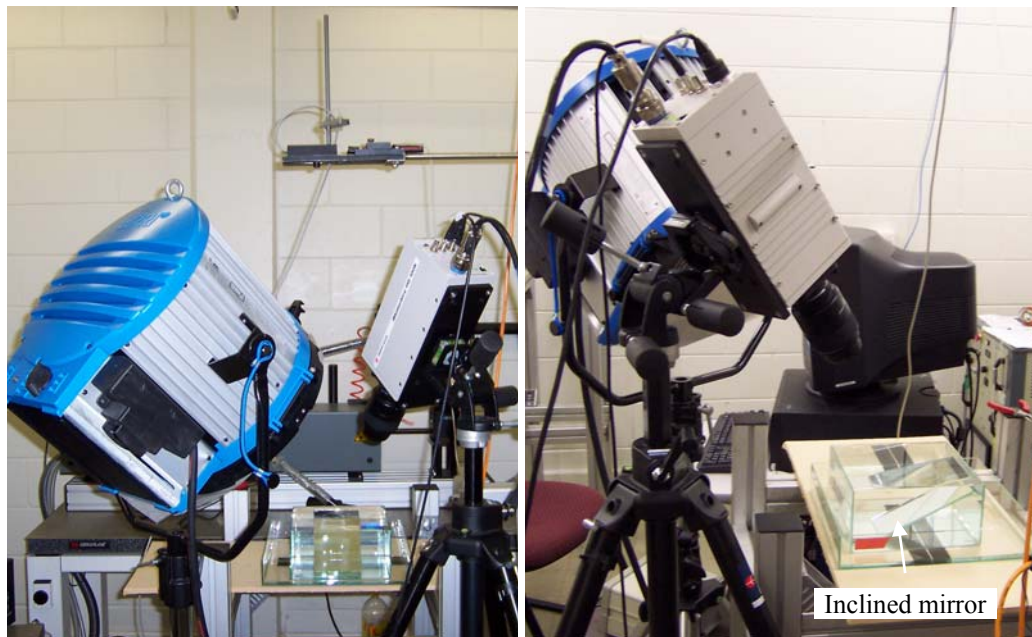


**Figure 2.8** Experimental setup of the camera in the down cavity configuration

### 2.3.3 Alignment and Calibration

Arguably, the most important task during experimentation is the alignment of the cameras and spatial calibration of the images. Any image that is largely out of focus cannot be relied on for accurate measurement. Alignment of the cameras was achieved by focusing both cameras onto a galvanized plate that was placed within the bath. The dropping arm was moved via the traverse system until the drop was impacting on the plate. After this was complete, a run was conducted to ensure everything was in focus. Further fine-tuning of the focal length and position of the dropping arm was made before a ruler was placed in the impact tank and recorded to capture an image for calibration. After the calibration was complete, a series of experiments was conducted. Care was taken during experimentation not to disturb the position of the cameras between experimental runs. A typical calibration image is shown in Figure 2.9.

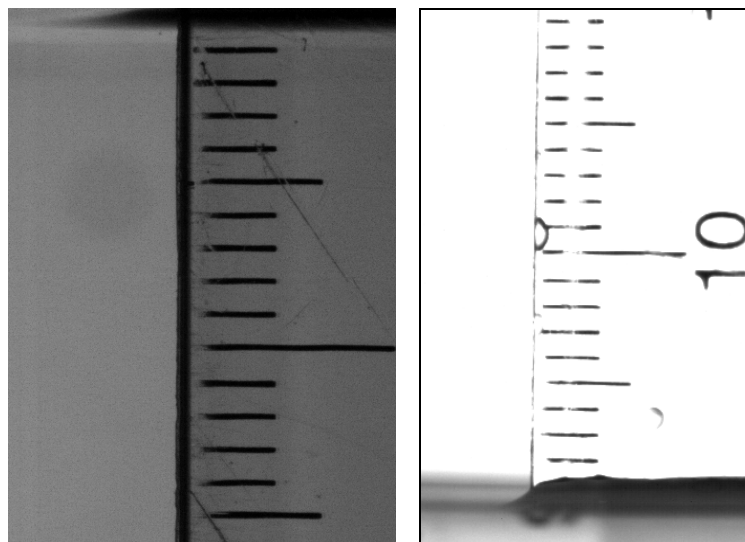


**Figure 2.9** An example of a calibration shot. (Left) Camera below surface (Right) Camera above surface

### 2.3.4 Determination of imaging parameters

When conducting any high-speed imaging several properties of the camera and lens are integral in ensuring the phenomena is captured appropriately. These parameters include

- Image resolution
- Framing rate
- Exposure time
- Lens aperture
- Lens magnification

Typical values of expected temporal and spatial ranges for liquid-liquid impacts are listed in Table 2.5. Examining Table 2.5 there exists an expansive range of values. If the camera is set to capture the largest cavity possible of 20 mm with a lens magnification of 1:1 or 12  $\mu\text{m}/\text{pixel}$  a horizontal resolution of 1666 pixels would be required. Since the camera cannot achieve such a wide field of view the camera magnification must be reduced to compensate. However, in doing so, information on the small entrapped bubbles and droplets from the high-speed jets will be lost. Furthermore, capturing images at the maximum resolution restricts framing rate, which in turn means the high velocity phenomena will not be captured. Thus, it is just not possible or feasible to conduct one experimental run and capture all the characteristics of the impact. Therefore, the magnification, framing rate and resolution must be individually tailored depending on the target phenomena resulting in the need for many different experimental runs to be conducted. The details of each experimental run can be found in section 2.5.

**Table 2.5** Expected ranges for various parameters

<b>Phenomena</b>	<b>Expected Value</b>
Cavity size (diameter)	3 – 20 mm
Impact drop size	2 – 5 mm
Impact drop velocity	1 – 4 m/s
Size of secondary drops	< 50 $\mu\text{m}$ – 4 mm
Velocity of secondary drops	0.5 – 20 m/s
Entrapped bubbles	< 10 $\mu\text{m}$ – 2 mm

In terms of exposure timing (the time the camera's sensor is exposed to light) the lowest value possible by the camera of 5  $\mu\text{s}$  was always used. The justification for using such short exposure is based on the requirement for sharp images regardless of the phenomena being studied. If the object moves more than 2 pixels while being exposed, the boundaries of drop will be blurred and unsuitable for analysis. Operating with a magnification of 12  $\mu\text{m}/\text{pixel}$ , a 5  $\mu\text{s}$  exposure provides clear and sharp images of flow features up to 4.8 m/s.

## 2.4 PIV

### 2.4.1 PIV configuration

In this project the first commercial High Framing Rate Particle Image Velocimetry (HFR-PIV) system by Dantec Dynamics was used to perform the PIV image capture and analysis. This unique system consists of two Redlake HG-100K cameras and a Lee Laser LDP-100MQG. This system uses the double-frame single pulse method of recording images and can perform both 2D and 3D PIV. However, in this study only 2D PIV was utilised. The double-frame single pulse method allows for the use of cross-correlation to compute the velocity vectors. Using individually exposed images removes some of the directional problems that can be present in other methods such as auto-correlation. However, on the downside, a complex timing mechanism is required to synchronise the cameras and laser. A diagram of how the timing works in this PIV system is shown in Figure 2.10.

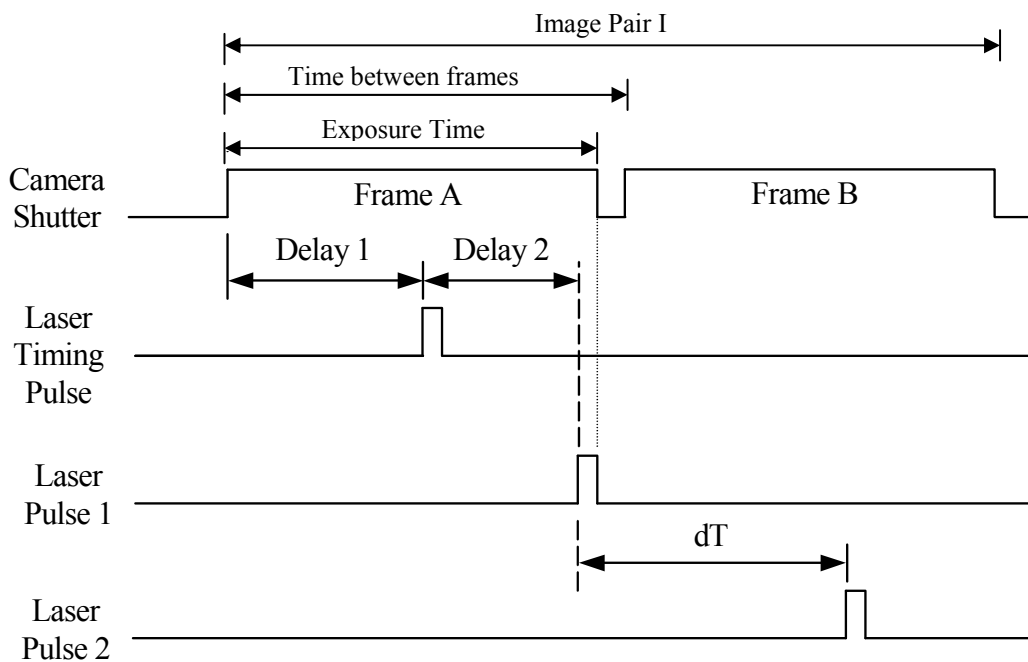


**Figure 2.10** Timing diagram for HFR-PIV system

The frame rate selected by the user determines the time between each frame. The time between the start of each frame is constant over the entire recording period. This holds true even for the time between the end of one image pair and the start of the next (*i.e.* The time between the start of Frame A and the start of Frame B in image pair I is the

same as the time between the start of Frame B in image pair I and the start of Frame A in image pair II). However, you cannot easily extract velocity fields between Frame B in image pair I and Frame A in image pair II due to the laser timing.

The nature of the diode pumped Nd:YAG laser requires an energy build up in the cavity prior to release. The longer the build up time the stronger the light pulse will be. Therefore, a timing signal must be sent to the laser to initiate energy build up before release. Delay 1 specifies the time between the start of the image pair and the time when energy build up begins. Delay 2 controls the rod charge up time for Frame A. By default the timings of the system are configured so that the first laser pulse occurs at the end of Frame A. This means that only one time delay value needs be changed as the other can be back calculated based on exposure time. However, both values can be changed to force the first laser pulse to occur before the end of Frame A. The real benefit of manipulating Delay 1 and Delay 2 is to control the light balance between laser pulses. If the average brightness between the two frames in an image pair are significantly different they may not correlate correctly. Therefore, Delay 1 and Delay 2 can be used to manipulate the brightness of each pulse by varying the energy build up time. Delay 1 is used to control the brightness of the pulse in Frame A while Delay 2 controls the brightness of the pulse in Frame B.

While Delay 1 and Delay 2 are essential in balancing the light levels between pulses the most important timing signal in the system is time delay between pulses ( $dT$ ).  $dT$  is used in the correlation process as the time between frames in each image pair. In general  $dT$  is not the same as the camera frame rate. Thus, as mentioned previously it is not easily to extract velocity fields between Frame B in image pair I and Frame A in image pair II. However, the benefit of having  $dT$  independent of the frame rate is that phenomena occurring faster than the framing rate can be captured in an image pair.

In the HFR-PIV system the timing signals between the laser and camera are handled via a proprietary signal timing box from Dantec along with a National Instruments PCI-660 timing in the host computer. The laser pulse duration is approximately 150 ns. A schematic diagram of the apparatus configuration for 2D-PIV is shown in Figure 2.11 along with a picture of the final experimental setup in Figure 2.11. Here the light arm is positioned beneath the liquid pool and at an angle such that the laser light sheet is

perpendicular to the camera's lens. In order to prevent excessive noise from being introduced into the PIV images imaging any out of plane particles needs to be avoided. This is generally achieved by adjusting the laser light sheet thickness contained on the light arm optics. However, the thickness adjuster was unable to provide a thin enough light sheet for the experiments conducted here. Therefore, two stripes of black masking tape approximately 2 mm apart were placed on the underside of the impact tank to create a slit. Dantec Dynamics Flow Manager software was used to handle all aspects of signal timing and acquisition. The final experimental apparatus setup is shown in Figure 2.12.

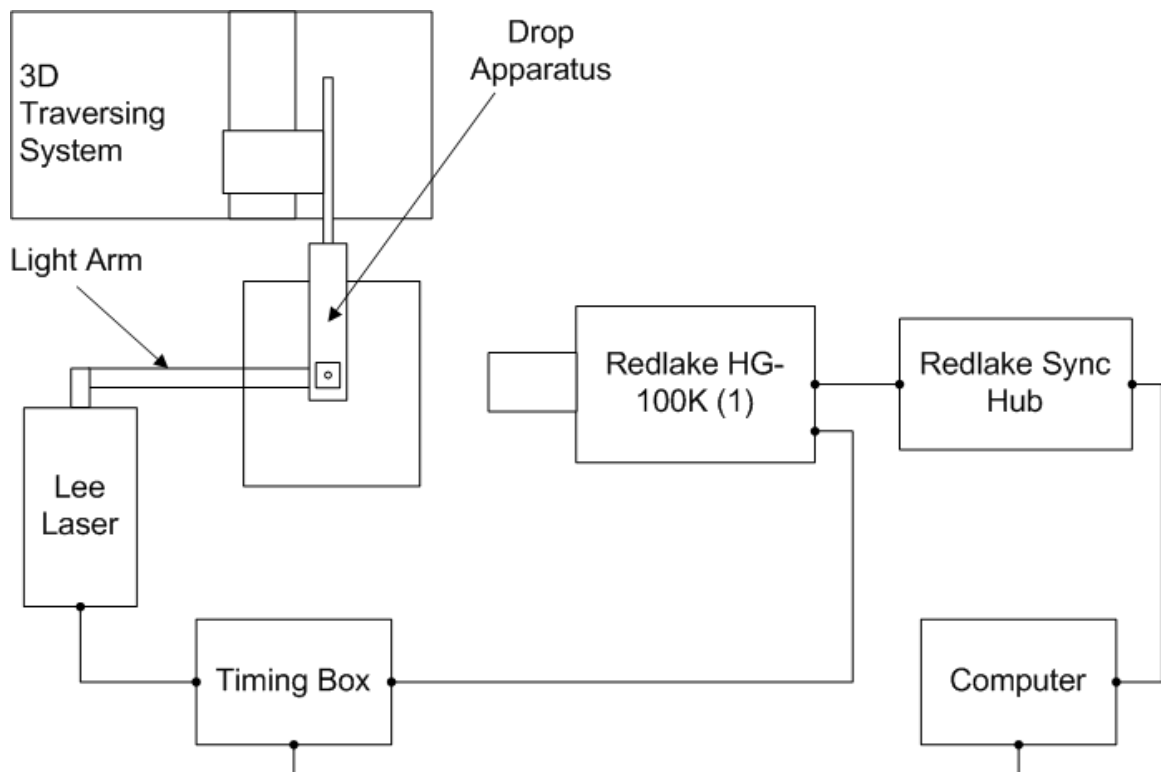


**Figure 2.11** Schematic of the apparatus for 2D-PIV

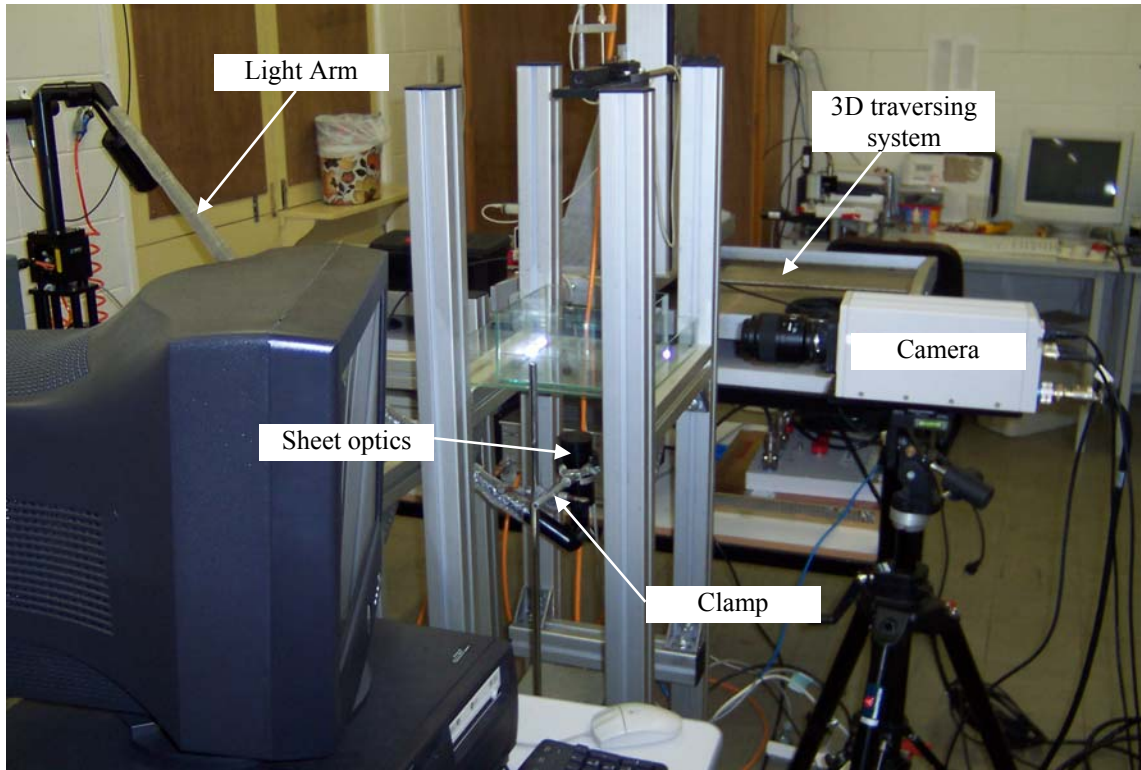


**Figure 2.12** Experimental setup for 2D PIV

#### 2.4.2 PIV Seeding

Numerous authors have described procedures and criteria for the appropriate selection of particles (Melling 1997 and Prasad 2000). Factors to be considered when selecting particles include, reflectivity, size, density and ability to follow the flow. Many of these properties are inter-related and one or more iterations through the following equations may be required to obtain the best particles for a given application. The first parameter to ascertain is the particle diameter. When a particle is illuminated by a light source diffraction will tend to spread the light out into a spot size governed by the diameter of the Airy disk diameter of the particle ( $d_{p,a}$ ).

$$d_{p,a} = 2.44(1 + M)f^{\#}\lambda_l \quad (2.1)$$

$d_{p,a}$  is governed by the magnification factor ( $M$ ), the f-number of the lens ( $f^{\#}$ ) and wavelength of the light ( $\lambda_l$ ). Combining  $d_{p,a}$  with the magnification factor and the actual particle diameter ( $d_p$ ), an effective size particle ( $d_{p,e}$ ) on the imaging plane can be found.

$$d_{p,e} = (M^2 d_p^2 + d_{p,a}^2)^{1/2} \quad (2.2)$$

For a satisfactory signal response in PIV it is ideal to have the imaged particle consisting of 4 pixels so a sub-pixel displacement can be found. Thus, the desirable effective diameter becomes equal to two pixel widths. Now  $d_{p,e}$  can be expressed in terms of the magnification factor and the width of a pixel on the sensor ( $w_s$ ).

$$d_{p,e} = \frac{2w_s}{M} \quad (2.3)$$

Combining equation 2.2 and equation 2.3 and rearrange in terms of the actual particle size ( $d_p$ ) the optimal particle diameter ( $d_{p,o}$ ) can be obtained.

$$d_{p,o} = d_p = \sqrt{\frac{4w_s^2 - M^2 d_{p,a}^2}{M^4}} \quad (2.4)$$

The second factor to consider in particle selection is the response time of the particle. The response time essentially governs how fast a particle can react to a change in velocity such that the particle moves with the flow. Raffel *et al.* (1998) suggest the response time of a particle to a step change in velocity at constant acceleration can be calculated using the following. The particle response time ( $\tau_p$ ) must be low compared to the time between laser pulses. The response time can be calculated as follows where  $\rho_p$  is the density of the particles,  $\rho_{pool}$  is the fluid density and  $\mu_{pool}$  is the viscosity of the pool fluid.

$$\tau_p = \frac{d_p^2 (\rho_p - \rho_{pool})}{18\mu_{pool}} \quad (2.5)$$

The particle settling velocity ( $U_{p,s}$ ) is given by the particle diameter, density difference between the particle and the surrounding media ( $\rho_{pool}$ ) and the viscosity of the media. Finally, the particle density must be low enough so that the settling velocity of the particle ( $U_{p,s}$ ) is small compared to the average velocity of flow field.

$$U_{p,s} = \frac{d_p^2 (\rho_p - \rho_{pool}) g}{18 \mu_{pool}} \quad (2.6)$$

A list of available particles for use in this thesis are shown in Table 2.6 along with their corresponding parameters.

**Table 2.6** Available particles with their corresponding properties

Particle Type	Manufacturer	Mean Diameter ( $\mu\text{m}$ )	Density (g/cc)	Response Time ( $\mu\text{s}$ )	Settling Velocity ( $\mu\text{m/s}$ )
Silver coated spheres	Potters Industries	89	2.6	1144	6907
Hollow glass spheres	Potters Industries	44	0.5	54	527
Polymer spheres	Degussa	45	1.016	114	18

The third parameter to ascertain is the seeding density of the particles. The seeding density depends on several factors including, the width of the light sheet, the width and height of each grid investigation area, the volume of the tank and the density of the particles themselves. Monte Carlo simulations suggest 12 particles per interrogation area ( $n_{p,i}$ ) is optimal with five being the minimum (Dantec Dynamics 2000). The number of particles required to seed the entire pool can be calculated as follows.

$$V_i = w_i^2 \cdot w_{pixel}^2 \cdot t_{sheet} \quad (2.7)$$

$$n_{p,pool} = \frac{V_{pool}}{V_i} \cdot n_{p,i}$$

Where  $V_i$  is the volume of an interrogation area,  $w_i$  is the width of an interrogation area in pixels,  $w_{pixel}$  is the width of a pixel on the imaging plane,  $t_{sheet}$  is the thickness of the laser light sheet,  $V_{pool}$  is the total pool volume and  $n_{p,pool}$  is the total number of particles required to seed the pool. Now the total mass of particles ( $m_p$ ) that needs to be mixed into the impact tank can be calculated.

$$m_p = V_{pool} \cdot \rho_p \cdot n_{p,pool} \quad (2.8)$$

Finally, the reflectivity of the particle needs to be considered. Hollow glass spheres have half the density of water but a lower reflectivity when compared to silver coated particles but silver particles are significantly heavier. Polymer particles have an almost exact density match for water but a very low reflectivity. Therefore, changing the particle type to maximise reflected light can change many of the important density related characteristics described previously. Furthermore, the different types of particles are only available in certain size ranges meaning it may not be even possible to obtain particles with the optimal diameter. Particle selection in PIV is a complex task and a certain degree of trial and error is required before the best particles can be found.

### **2.4.3 PIV implementation**

Many compromises on the optimal values discussed above had to be made in order to make PIV liquid-liquid impacts to work and will be discussed now. The first series of tests conducted to see if HFR-PIV was even possible in this application revolved around investigating the whether the optical transmission of the particles was sufficient. Initially the camera was configured with an f-number of 11, magnification of 1:1, the laser light sheet thickness of 2 mm and framing rate set to 3000 FPS. Silver coated spheres were added to the pool and stirred to distribute them. The silver coated spheres performed exceptionally well in terms of reflected light. However, in the five or so seconds it takes for the free surface to settle and activate the laser and cameras, most of the particles had fallen well below the area of interest near the surface. Hollow glass spheres were tested next and they had the reverse problem to the silver coated spheres. Rather than sinking, these particles rose too rapidly and formed a thick layer of particles on the free surface. Finally, the almost neutrally buoyant polymer spheres were trialled. These particles performed exceptionally well in regards to staying within the target area but performed extremely poorly in terms of light reflected. While the polymer particles transmit low light levels they were the only particles capable of residing in the cavity formation zone so they were selected to perform all of the PIV experiments in this thesis.

It is quite clear that the main problem now in carrying out the PIV imaging is a lack of light being returned to the cameras sensor. In standard rate PIV (30 Hz) the exposure times are high and laser pulse energy are quite high. In HFR-SPIV the opposite problem

exists, very low exposure times (dictated by the framing rate) and low energy per pulse (due to the high repetition rate). The most obvious solution to increasing reflected light levels is to increase the output power of the laser. However, a curved free surface, like the cavity formed from a liquid-liquid impact, has highly reflective properties, which cause significant light scatter. It was found that during the cavity collapse phase if the supply amperage was pushed past 13 amps strong light flares would saturate the whole image with light making the images impossible to analyse. Therefore, the first compromise to be made was decreasing the f-number of the lens to 2.6 to allow more light into the sensor. In changing the aperture of the lens the light sheet thickness needs to be adjusted to prevent excessive out of focus particles from being captured. With these settings the required light sheet thickness would ideally be 0.06 mm. This is impossible to achieve in practice so the slit restricted the sheet thickness was reduced to approximately 1 mm. Furthermore, the magnification factor was reduced to approximately 0.5 so the depth of field becomes slightly larger to 0.1 mm. While this measure had a dramatic increase on lighting levels the framing rate was reduced to 2000 FPS to increase the exposure time even further.

The last problem encountered during HFR-PIV experimentation was actually seeding the area of interest with particles. It was found that filling the entire pool with the required particles to reach the optimal seeding density (equation 2.8) significant amounts of light was blocked. Therefore, a technique was employed to inject a pre-made solution of particles in the target area before recording. The particles were ultrasonically vibrated to obtain an even dispersion before being injected. Shortly after the particles were placed in the pool recording was initiated. In summary there are many practical challenges associated with conducting HFR-PIV. The main problem encountered was insufficient lighting. For HFR-PIV in general this problem can be overcome by producing more powerful lasers. However, in this specific application if too much power is used reflections can seriously degrade image quality. Finally, the ideal parameters that can be calculated should only be used as a guide for a first attempt at HFR-PIV. Many of the light restriction issues mean significant compromises are required to make HFR-PIV to work in practice.

## 2.5 Experiment Lists

All the experimental runs referred to in this thesis are shown in Table 2.7, Table 2.8 and Table 2.9. The purpose of each experiment run is described along with the regimes with the relevant framing rate and resolution information.

**Table 2.7** Experiments conducted with 33G needles

Study Item	Purpose	Regime	Camera Settings
1	Adding new phenomena to drop splash map. Put limits on existing and new phenomena.	All	<ul style="list-style-type: none"> <li>• Below 2000 FPS 1024×768</li> <li>• Above 3000 FPS 800×600</li> </ul>
2	Examine vortex ring formation by dying the impacting drop	Composed	<ul style="list-style-type: none"> <li>• Below 6000 FPS 512×416</li> <li>• Above 3000 FPS 800×600</li> </ul>
3	Examine in detail thin high-speed jets	Primary bubble entrapment	<ul style="list-style-type: none"> <li>• Above 10000 FPS 288×416</li> <li>• Below 3000 FPS 800×600</li> </ul>
4	Study of the flow field around the evolving cavity using PIV	All	<ul style="list-style-type: none"> <li>• Below 2000 FPS 640×480</li> </ul>
7	Using extremely high speed to study the cavity retraction and bubble entrapment	Pre-entrapment and Primary bubble entrapment	<ul style="list-style-type: none"> <li>• Below 40000 FPS 128×128</li> <li>• Above 5000 FPS 416×560</li> </ul>
8	Using extremely high framing rates to examine the snap off process	Pre-entrapment and Primary bubble entrapment	<ul style="list-style-type: none"> <li>• Below 81595 FPS 64×48</li> <li>• Above 5000 FPS 416×500</li> </ul>
9	Looking into the cavity to see the details obscured when examining the profile of the cavity	All	<ul style="list-style-type: none"> <li>• Above 8000 FPS 480×368</li> </ul>
11	Examination of the jetting regime before bubble entrapment	Pre-entrapment	<ul style="list-style-type: none"> <li>• Below 6000 FPS 512×416</li> <li>• Above 3000 FPS 800×600</li> </ul>
12	Close examination of the jet in bubble	Primary bubble entrapment	<ul style="list-style-type: none"> <li>• Below 20000 FPS 192×192</li> <li>• Above 3000 FPS 800×600</li> </ul>

**Table 2.8** Experiments conducted with 26g needles

<b>Study Item</b>	<b>Purpose</b>	<b>Regime</b>	<b>Camera Settings</b>
1	Adding new phenomena to drop splash map. Put limits on existing and new phenomena.	All	<ul style="list-style-type: none"> <li>• Below 4000-3000 FPS variable res.</li> <li>• Above 4000-5000 FPS variable res.</li> </ul>
2	Detailed examination of the jetting regime before bubble entrapment	Pre-entrapment	<ul style="list-style-type: none"> <li>• Below 3000 FPS 736×632</li> <li>• Above 5000 FPS 448×592</li> </ul>
3	Attempting to gather more information on the origins of the thin jet by looking into the cavity	Primary bubble entrapment	<ul style="list-style-type: none"> <li>• Above 5000 FPS 640×480</li> </ul>
4	Using dyed drops to see the flow field across the entire range	All	<ul style="list-style-type: none"> <li>• Below 3000-2500 FPS variable res.</li> <li>• Above 5000-3000 FPS variable res.</li> </ul>
5	Investigating to see if a region of double bubble entrapment exists	Primary bubble entrapment	<ul style="list-style-type: none"> <li>• Below 3000 FPS 800×592</li> <li>• Above 5000 FPS 288×512</li> </ul>

**Table 2.9** Experiments conducted with 20g needles

<b>Study Item</b>	<b>Purpose</b>	<b>Regime</b>	<b>Techniques to be used</b>
1	Adding new phenomena to drop splash map. Put limits on existing and new phenomena.	All	<ul style="list-style-type: none"> <li>• Below 2000 FPS 1024×768</li> <li>• Above 3000 FPS 800×600</li> </ul>
2	Detailed examination of the jetting regime before bubble entrapment	Pre-Entrapment	<ul style="list-style-type: none"> <li>• Below 6000 FPS 512×416</li> <li>• Above 3000 FPS 800×600</li> </ul>
3	Investigation into the formation and rupture of thin gaseous films	Post-Entrapment	<ul style="list-style-type: none"> <li>• Below 27175 FPS 224×160</li> <li>• Above 5000 FPS 448×592</li> </ul>
4	Examine vortex ring formation by dyeing the impacting drop. For comparison with PIV data.	Composed	<ul style="list-style-type: none"> <li>• Below 6000 FPS 512×416</li> <li>• Above 3000 FPS 800×600</li> </ul>
5	Using PIV to investigate the flow resulting from vortex ring formation and bubble entrapment	Composed, Pre-Entrapment and Primary bubble entrapment	<ul style="list-style-type: none"> <li>• Below 3000 FPS 800 × 600</li> </ul>

### 2.5.1 Repeatability

In this study no direct repeat studies were conducted. However, very similar runs were conducted out often looking at specific phenomena. The repeatability of these experiments can be judged by examining the impact conditions and regimes of a drop formed by the same size needle from the same height. One such example is a drop falling from 140mm with 33g needles. The impact conditions of this drop from five different runs is shown in Table 2.10.

**Table 2.10** Repeatability of drops

<b>Study Number</b>	<b>Drop Diameter (mm)</b>	<b>Drop Velocity (m/s)</b>
01-140-33g	2.0438	1.79
03-140-33g	2.036	1.78
07-140-33g	2.1049	1.78
08-140-33g	2.0691	1.78
11-140-33g	1.994	1.78
Max variation	5.3%	0.5%

The variation in drop diameter can be attributed to oscillations and errors involved in the diameter estimation procedure as will be discussed in the next section. The drop velocity is far more accurate due to the fact that the centroid of the drop is tracked. The 140mm-33g impact falls on the border of the pre-entrapment jetting and primary bubble entrapment regimes. All cases of the 140mm-33g impacts fell within the pre-entrapment jetting regime while impacts from a slightly higher height of 160mm all fell within the primary bubble entrapment regime.

## 2.6 Analysis Techniques and Errors

### 2.6.1 High speed video

In this thesis, over 400 individual impacts were recorded resulting in over 400 000 images equating to approximately 100 GB of data. With this volume of data to analyse an easy and accurate method of determining drop size and velocity was required. To achieve this goal a MATLAB program with a graphical user interface (GUI) was developed to extract drop velocity and diameter. A screenshot of the program is shown in Figure 2.13.

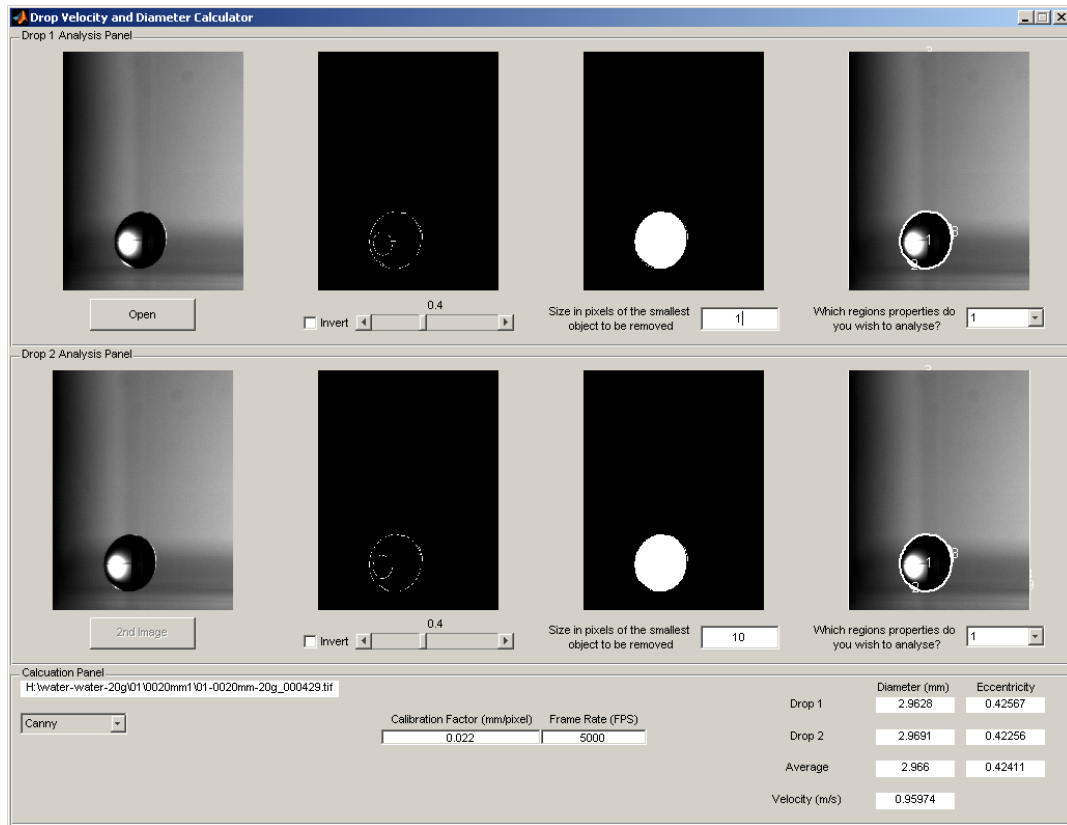


**Figure 2.13** Screenshot of the drop size and velocity calculator

The program functions as follows: The user selects the image they wish to analyse and then that image and the following image in the sequence is imported and displayed in the first box. Both images are then analysed using the desired edge detection method. Five edge detection methods were implemented using the built in MATLAB functions. Of all the methods tested, the Canny edge detector was found to perform exceptionally well regardless of image quality and was therefore used almost exclusively. The detected images were displayed in the second image box. After the edges of the objects in the image were identified 2D areas or regions were formed. Regions smaller than the user specified value were deleted and the remaining regions displayed in image box three. The final step in processing the images involves taking the original image and overlaying the detected edges while a number was placed at the centroid of each region identified. This mechanism gives the user feedback so they can select which regions properties to investigate.

To calculate the drop's diameter, a function in MATLAB was utilised to convert the area of the region to an equivalent circular area. This is not the ideal method of calculating drop diameter, especially if the drop is oscillating. Drop oscillation in three dimensions can either increase or decrease the area presented to the camera depending on oscillation phase. Therefore, the most accurate method is to perform an integration of the drop profile, extract a solid of revolution based on the solid, then back calculate an equivalent sphere diameter based on this volume. However, time and technical restrictions prevented this method from being implemented. Therefore, a brief investigation was carried out to ensure the method of converting a 2D area into an equivalent area was valid for this study. The largest error in drop diameter will come from highly oscillatory drops. Large drops falling short distances will exhibit the largest oscillations. Therefore, a drop from a 20g needle falling 20 mm was selected as the worst-case scenario. The drop was tracked over 40 consecutive frames and diameter data extracted. In this time the drop underwent a full oscillation from fully prolate to oblate then back to prolate. The smallest measured diameter was 3.14 mm, largest diameter 3.26 mm giving a maximum variation of 3.7%. Therefore, the method used here in calculating drop diameter is valid if the drop size remains small.

The velocity of the impacting drop was simply calculated by tracking the centroid of the region between consecutive frames. Velocity calculations are largely independent of drop oscillations. The velocity calculation were so accurate that velocity changes of drops falling from a height difference of 5 mm could be detected. The MATLAB source code for this program can be found in Appendix A.

When the Canny edge detector could not discern drop edges and thus calculate drop diameter and velocity, Photoshop was used to manually extract these values. In Photoshop, the drop diameter was approximated with an equally sized circle. The centre coordinate of the circle was used to measure its displacement and thus used to determine drop velocity. However, using this technique is far less accurate than using the MATLAB program. Drop diameter could only be estimated to within 1 pixel not the sub pixel accuracy given by the MATLAB program. Furthermore, if the release height of the drop varied by less than 10 mm no velocity difference could be detected.

### 2.6.2 PIV analysis techniques

With all PIV images, a degree of post processing is required before any meaningful data can be produced. For the images collected in this study several post processing steps were taken before the final velocity fields were produced. A raw image of a cavity collapsing is shown in Figure 2.14.

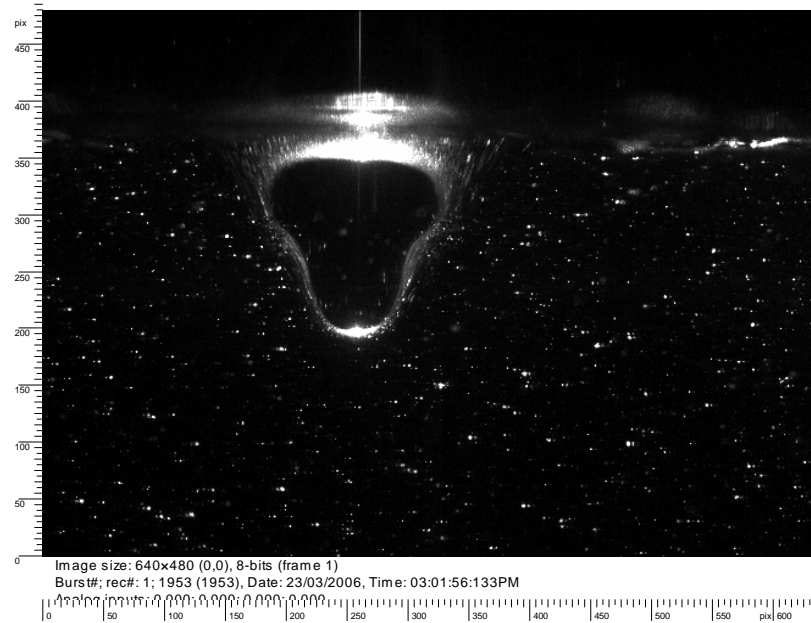


**Figure 2.14** Raw PIV image of a cavity collapsing

In Figure 2.14 there is a significant amount of reflections due to the cavity and free surface creating bright spots on the image. If these spots are not removed they can produce erroneous vectors in the correlation process. Therefore, the region above the free surface and cavity are masked. The mask created for this image pair is shown in Figure 2.15. The now masked raw image is shown in Figure 2.16.

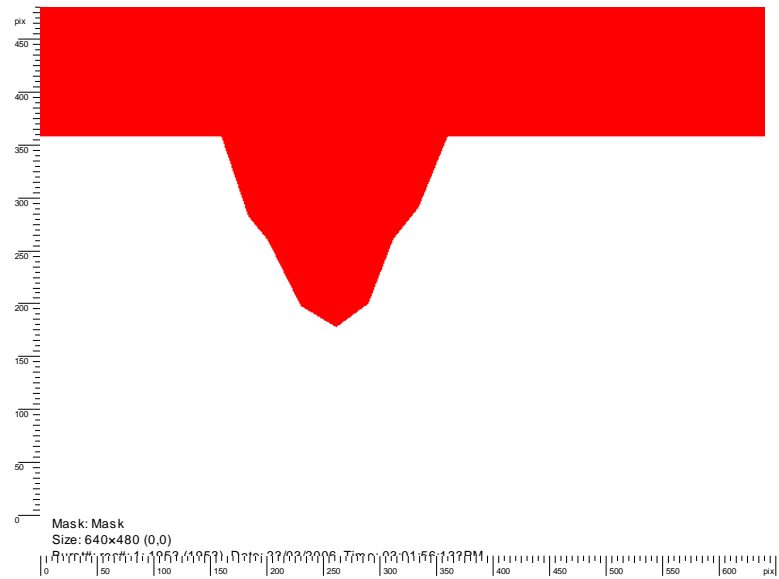


**Figure 2.15** Mask used to exclude the free surface and cavity from correlation

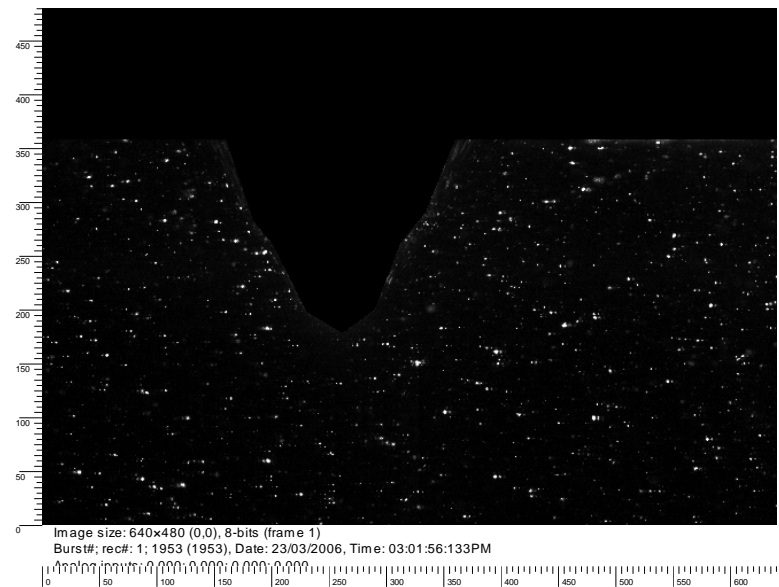


**Figure 2.16** Masked raw image

Having obtained a suitable image pair, cross-correlation can now be performed. Many different parameters for the cross-correlation were trialled. Interrogation areas of  $64 \times 64$  with differing overlaps were tested but were unable to resolve some of the finer details of the flow. Next  $32 \times 32$  interrogation areas were used and gave satisfactory results. Most of the localised phenomena near the cavity could be detected. Finally,  $16 \times 16$  interrogation areas were investigated but the relatively low seeding density meant the correlations were quite weak and produced many erroneous vectors. The best overall

solution was found to be  $32 \times 32$  interrogation areas with a 50% overlap. A typical raw cross-correlation is shown in Figure 2.17.

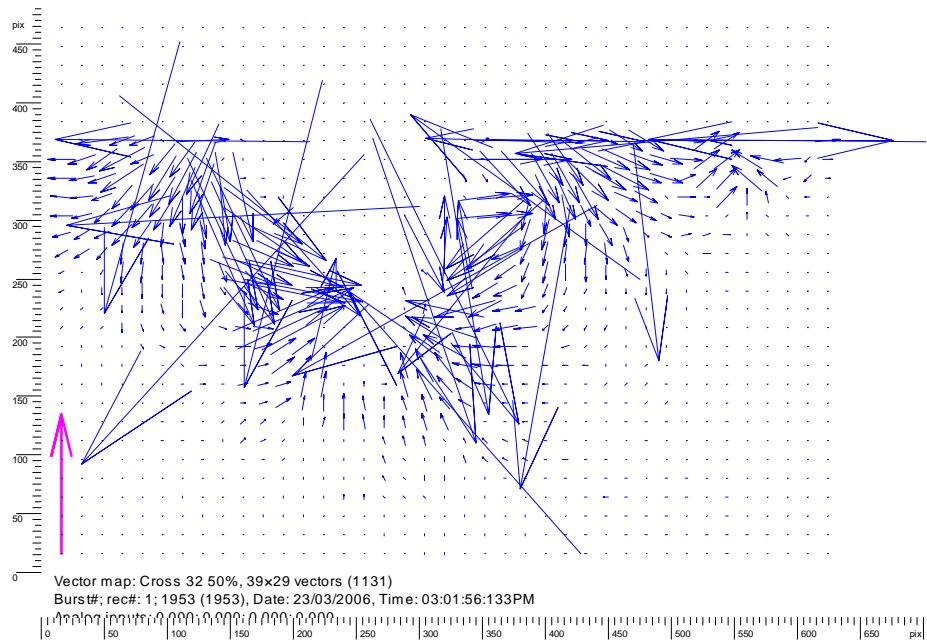


**Figure 2.17** Raw cross-correlation image

Examining Figure 2.17 it can be seen how there are many erroneous vectors present. The next step in the post processing procedure is to remove these vectors. A range validation was used to remove vectors with a velocity magnitude less than 0.001 m/s. These low velocity vectors are due to noise. Next, a moving-average validation was applied to the correlation. A moving-average essentially removes any vectors that have a magnitude or direction significantly different from the vectors surrounding it. The removed vector is replaced by a vector that is estimated by magnitude and direction of its neighbours. The moving-average validation is shown in where the green vectors are substituted vectors.

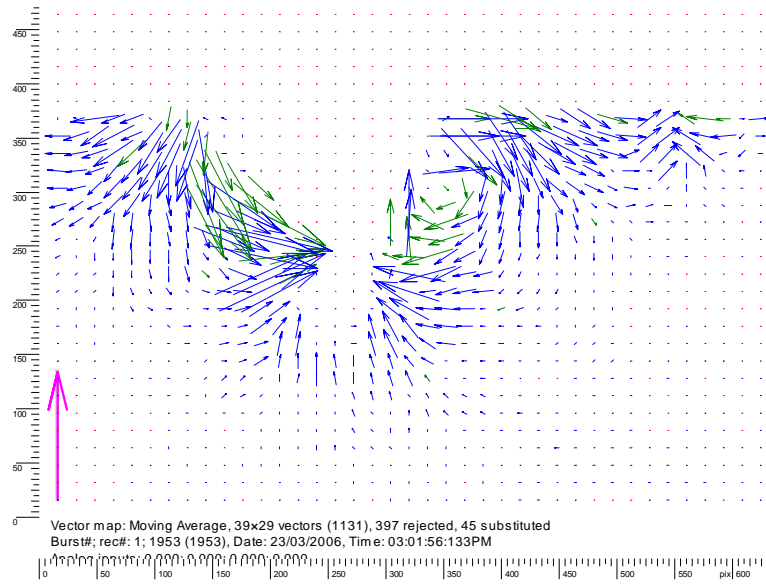


**Figure 2.18** Vector map after moving-average has been applied

The final step of the correlation process is to apply an average filter. The average filter takes a vector and replaces it with the weighted average of its neighbours. In this way the final velocity field is smooth and free of any discontinuities. The final velocity field after post processing is shown in Figure 2.19. The PIV results displayed in this thesis consist of the final post-processed velocity field overlaid on the raw image so the reader can relate the flow field to the stage of cavity formation or collapse being addressed.

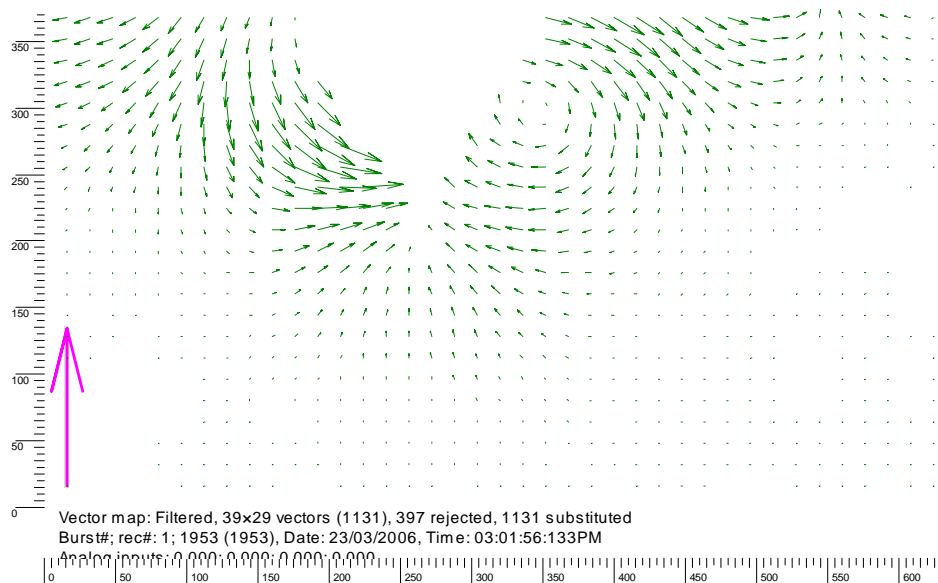


**Figure 2.19** Final post-processed velocity field

Equipped with a final velocity field, other quantities such as vorticity, scalar maps and streamlines can be calculated. Figure 2.20 is a scalar contour map of the velocity magnitude and Figure 2.21 shows a vorticity contour map.

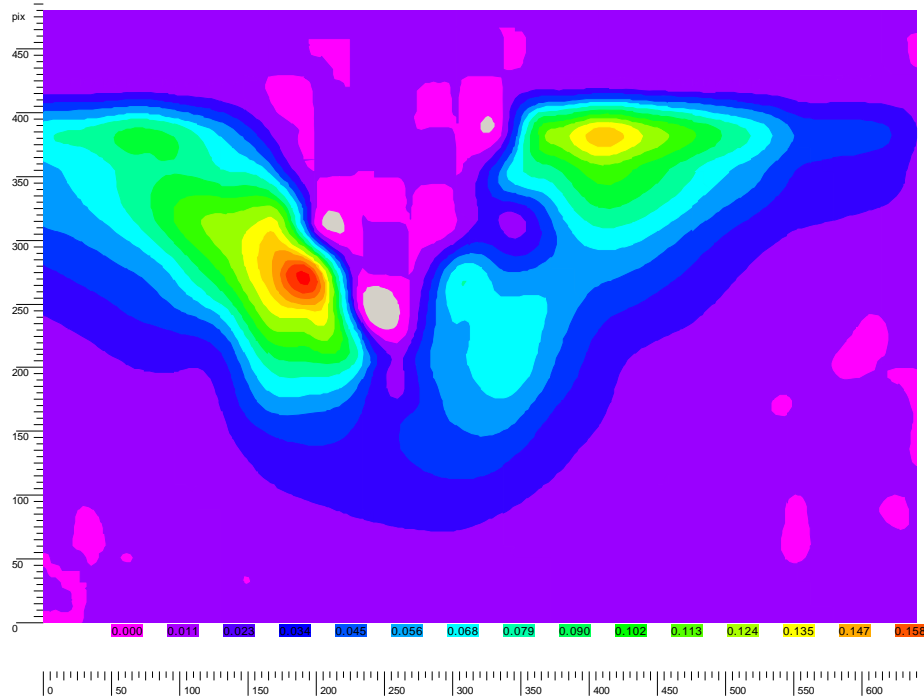


Figure 2.20 Scalar velocity map

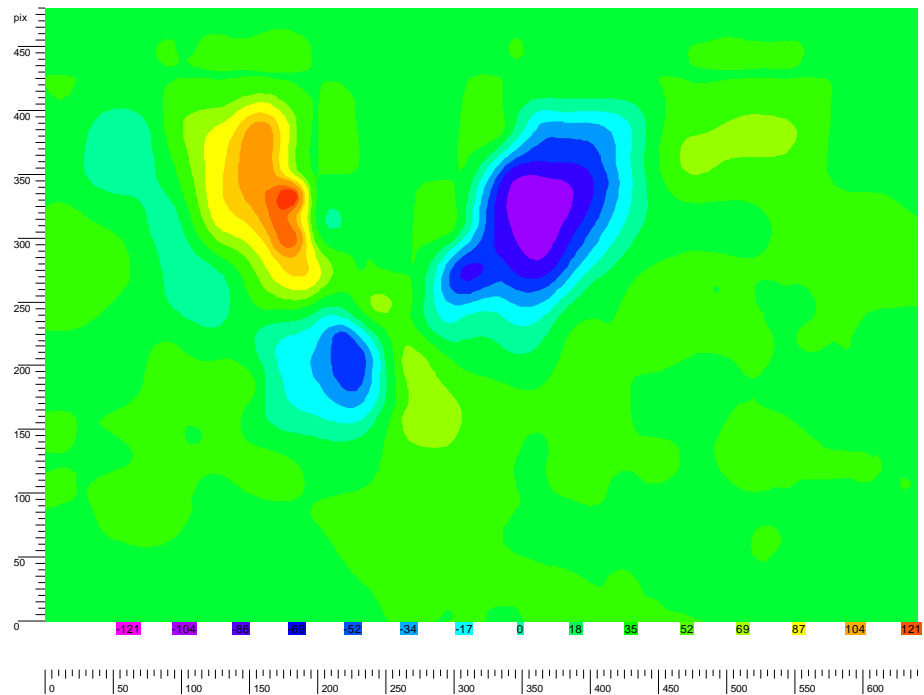


Figure 2.21 Vorticity map

### 2.6.3 PIV errors

Errors in PIV experiments are introduced via uncertainty associated with laser timing, magnification calibration, and bias error. The magnification factor was estimated by photographing and scaling a distance from a vernier. The error in this process is approximately 1 pixel over the 1000 pixels  $\approx 0.1\%$ . The second source of error arises from the timing of the laser pulses. The maximum error here arises from the synchronisation of the cameras to the laser pulse, the maximum is estimated to be  $2.6 \mu\text{s}$  or  $\approx 0.6\%$  of the time between pulses for a pulse delay of  $492 \mu\text{s}$ . Finally, the most significant source of error is due to the sub-pixel displacement estimation of the particles or bias error. In this study, the maximum bias error is estimated to be in the order of  $\pm 0.042 \text{ m/s}$  or  $\approx 10\%$  of the maximum velocity detected, increasing with decreasing particle displacement. The uncertainty and bias error associated with the calculation of the vorticity is given by the uncertainty from the centre differencing numerical scheme. Using the maximum error associated with the velocity calculation, the maximum error in the vorticity calculations is estimated to be  $30\%$ . In HFR-PIV the accuracy of the results are highly dependant on the sub-pixel accuracy. Therefore, it is recommended that in any HFR-PIV the imaged particle size be quite large (*i.e.* 6-7 pixels).

## 2.7 Summary

Detailed descriptions of the experimental apparatus used in this study have been outlined. The techniques used to analyse the data have also been described along with the expected errors in the analysis. A list of experiments was also formulated that will provide data to address the objectives identified in Chapter 1. Thus, the focus now turns to the first experimental results gathered from this study. The first set of experiments carried out in this study involved a systematic study of the splashing behaviour over a board of impact velocities and needle sizes. New and existing flow behaviour have been identified and classified from these experiments and are summarised in Chapter 3.